The Dissertation Committee for David Purtseladze Certifies that this is the approved version of the following dissertation

Non-reciprocity in Metamaterials

Committee:

Richard Fitzpatrick, Supervisor

Alexander Khanikaev, Co-supervisor

Andrea Alù

Alexander Demkov

Arno Bohm

Non-reciprocity in Metamaterials

by

David Purtseladze

DISSERTATION

Presented to the Faculty of the Graduate School of
The University of Texas at Austin
in Partial Fulfillment
of the Requirements
for the Degree of

DOCTOR OF PHILOSOPHY

UNIVERSITY OF TEXAS AT AUSTIN
December 2017

Dedicated to my parents.

Acknowledgments

The work presented in this dissertation would not be possible without the help and support of many people. I would like to thank professor Alex Khanikaev for providing invaluable knowledge, support and motivation for my Ph.D program. Alex generated almost all ideas that eventually become projects I worked on, taught me how to use COMSOL, TCMT and gave me valuable life advice. I would like to thank my thesis committee for feedback and support. Thanks to Dr. Keto for being always being available providing assistance. Thanks to prof. G. Shvets for guiding my projects in the first few years of my graduate studies. Thanks to current and former graduate students that worked with and became an integral part of this dissertation. Especially H. Mousavi for helping me learn very specific physics software, N. Arju for providing the experimental data for our projects and hours of valuable discussions. Thanks to G. Kelp for being always being supportive when things were not working out. Thanks to T. Ma and K. Lai for providing excellent working atmosphere.

I am deeply indebted to my parents. Without their continuous support and proper upbringing I would have never made this far. Thanks to family for always being there supporting me even though we are oceans apart.

I am leaving out more people than I was able to include in this brief text.

Abstract

Non-reciprocity in Metamaterials

David Purtseladze, Ph.D.
The University of Texas at Austin, 2017

Supervisors: Richard Fitzpatrick, Alexander B. Khanikaev

Non-reciprocal devices have played a crucial role in photonic and microwave applications. Conversion of polarization state of light, unidirectional light propagation emerge due to various symmetry reductions. In the first part of my talk I will propose a design for unidirectional leaky meta-waveguide based on Fano resonant metasurfaces deposited on top of ferrite. Later I will talk about Klein tunneling in photonic graphene, the unimpeded transmission of massless particles through a potential barrier owing to their Dirac-like dispersion.

Contents

List of Figures

List of Abbreviations

AFM	Atomic force microscope
BM	Beam splitter
CD	Chiral dichroism
CDA	Chiral dichroism in absorption
CDT	Chiral dichroism in transmission
COMSOL	Common solutions
DCF	Double continuum fano
FRAMM	Fano resonant asymmetric metamaterials
HNC	horizontal nanorod coupler
LCP	Left circularly polarized
MD	Magnetic dipole

PE	Polyethylene
PM	Parabolic Mirror
PRM	Phase retardation mirror
PSPD	Positionsensitive photodetector
QCL	Quantum cascade laser
QWP	Quarter wave plate
RCP	Right circularly polarized
SI	Spatial inversion
s-SNOM	Scattering scanning nearfield optical microscopy
TCMT	Temporal coupled mode theory
TE	Transverse electric
TM	Transverse magnetic
TR	Time reversal

1 Section A: Introduction

1.1 Metamaterials

Metamaterials are artificially engineered materials that exhibit unique properties that are not found in nature. Composed from structures of subwavelength scale arranged in certain patterns, metamaterials demonstrate strong resonant coupling to electromagnetic field due to collective effects. The field of metamaterials has a variety of applications; materials with both negative permeability and permittivity can be used to accomplish superresolution in optical imaging [1, 2]. Non-reciprocal optical response: one-way propagation[3, 4], slow light[5, 6, 7], polarization conversion[8, 9]. Realization of these applications is often hindered by strong dispersion and losses due to resonant nature of the effects. Another obstacle is difficulty in fabrication of 3 dimensional metamaterials. However 2D metamaterials (metasurfaces) are available for fabrication via lithography and nanopatterning. Another advantage of metasurfaces over bulk metamaterials is reduced ohmic losses. In this dissertation I will focus on metasurfaces.

2 Section B:Polarization conversion

2.1 Introduction

Polarization state of an electromagnetic wave is an intrinsic property that determines the plane of oscillation of electric field vector as the wave propagates through space. A linearly polarized wave has its electric and magnetic fields oscillate in planes that are orthogonal to each other. Circularly polarized light represents a superposition of two linearly polarized waves propagating in the same direction with the phase shift of $\pi/2$. In a circularly polarized wave the electric field vector has a constant magnitude but its direction rotates with time. The direction of this rotation defines its handedness.

For many electromagnetic and photonic applications it is desirable to be able to efficiently convert between different polarization states of light. Through selective manipulation of two orthogonal linear polarization states it is possible to adjust the phase between them without loss of transmission, however devices operating on this principle have a disadvantage of being bulky and narrow band. Narrowband polarization converters between linear and circular polarization states (quarter waveplates), or linear polarization rotation (half wave plates) with limited efficiency (up to 50%) have been realized using single-layer metasurfaces[8, 10, 11].

Circularly polarization states are of great interest because of their symmetries. For example, the same circularly polarized wave appears as two opposite polarization states from the perspective of the source and the receiver. Reversal of polarization state also occurs when a circularly polarized wave is reflected. These effects can be easily understood by inspecting a time reversal transformation of Maxwell's equations: $t \to -t, \vec{E} \to \vec{E}$, $\vec{B} \to -\vec{B}$. These properties of circularly polarized allow for extraordinary interaction with chiral structures.

Chirality is a geometrical property of objects that emerges from their intrinsic asymmetry. A chiral object is distinguishable from its mirror image and cannot be superimposed on it through a series of translations and rotations. The word Chiral originates from the Greek word $\chi\varepsilon\iota\rho$ that means hand. Organic molecules found in nature happen to be predominantly chiral. Similarly, light waves can also occur as left and right circularly polarized (LCP and RCP respectively). Chiral materials that differently interact with LCP and RCP light may cause rotation of the polarization state of light. Polarization rotation occurs because the effective refractive index $n = n' + in''$ of the material is different for LCP and RCP light. The real part of the refractive index n' is responsible for phase accumulation while the imaginary part n'' for Ohmic losses. Unequal n' for RCL and LCP light results in birefringence, whereas unequal n'' results in different absorption rate.

Because naturally occurring materials are weakly chiral, artificial metamaterials have been designed to exhibit strong chiral response. One of the straight forward ways of achieving chirality is to mimic helical molecules[12, 13]. However it has been shown that metasurfaces a few nanometers thick can be used to achieve circular dichroism. This effect is largely due to high Ohmic losses at the resonant frequencies. It has been theoretically shown that fully two dimensional metamaterials cannot be circularly dichroic in the absense of Ohmic losses [8].

2.2 Circular dichroism in lossy planar metasurfaces

In this study the structure in question produces drastically different electromagnetic field distribution for RCP and LCP light which results in unequal absorption (energy dissipation). Each unit cell consists of two resonant elements: the vertical dipole antenna, and the monopole antenna attached to a vertical wire running across the unit cell.

In the absence of near field interaction, the plasmonic resonances of unperturbed antennas occur at ω_y^0 and ω_x^0 respectively.

The mathematical model describing the interaction of antennas with each other and the incident light:

$$\frac{d}{dt}\begin{pmatrix} a_x \\ a_y \end{pmatrix} + i\begin{pmatrix} \omega_x & -\kappa \\ -\kappa & \omega_y \end{pmatrix}\begin{pmatrix} a_x \\ a_y \end{pmatrix} = \begin{pmatrix} \tau_{x;rad}^{-1} E_x \\ \tau_{y;rad}^{-1} E_y \end{pmatrix} \tag{2.1}$$

The set of equations are obtained from the temporal coupled mode theory(TCMT). $a_{x,y}$ are the amplitudes of electric dipole moments and $\omega_{x,y}$ are the complex valued amplitudes that take into account radiative ($\tau_{x,y;rad}^{-1}$) and Ohmic ($\tau_{x,y;Ohm}^{-1}$) losses:

$$\omega_{x,y} = \omega_{x,y}^0 + i(\tau_{x,y;rad}^{-1} + \tau_{x,y;Ohm}^{-1}) \tag{2.2}$$

The reflectivity matrix can be obtained from reciprocal nature of modes coupling to incident light:

$$-\begin{pmatrix} \tau_{x;rad}^{-1/2} & 0 \\ 0 & \tau_{y;rad}^{-1/2} \end{pmatrix} \begin{pmatrix} a_x \\ a_y \end{pmatrix} = \mathbf{R} \begin{pmatrix} E_x \\ E_y \end{pmatrix} \tag{2.3}$$

While the transmission matrix is given by: $\mathbf{T} = \mathbf{I} + \mathbf{R}$ where $\mathbf{I}$ is a unity matrix.

Circularly polarized light incident normal to the metasurface can be described with following vectors:

$$\begin{pmatrix} E_x \\ E_y \end{pmatrix}_{LCP} = \frac{1}{\sqrt{2}} \begin{pmatrix} 1 \\ i \end{pmatrix}, \begin{pmatrix} E_x \\ E_y \end{pmatrix}_{RCP} = \frac{1}{\sqrt{2}} \begin{pmatrix} 1 \\ -i \end{pmatrix} \tag{2.4}$$

Polarization conversion arises when transmission coefficients for RCP and LCP light are different. Chiral dichroism in transmission (CDT) $\Delta T_{CD} = T_R - T_L$ can be obtained from:

$$\Delta T_{CD} = -\frac{2\kappa}{(\tau_{x;rad}\tau_{y;rad})^{3/2}} \left| \frac{1}{\kappa^2 - (\omega - \omega_x^0)(\omega - \omega_y^0)} \right|^2 \left(\frac{\tau_{x;rad}}{\tau_{x;Ohm}} - \frac{\tau_{y;rad}}{\tau_{y;Ohm}} \right) \tag{2.5}$$

Several observations can be made from equation (2.5): (a) It is not possible to have CDT without losses in at least one of the antennas. (b)The CDT is maximized when the ratio of radiative loss to Ohmic loss is vastly different ($\tau_{x;rad}/\tau_{x;Ohm} >> \tau_{y;rad}/\tau_{y;Ohm}$) and the resonances are spectrally close ($\omega_x^0 \approx \omega_y^0$)

The design of the structure meets these conditions because the monopole antenna's mode is known [9] to have much longer lifetime than that of dipole antenna's mode and the resonant frequencies can be tuned to be spectrally close.

COMSOL simulations were carried out for the metasurface shown in Fig. 2.1 (a). In the case without Ohmic losses, transmission is identical $T_R = T_L$ despite having drastically different electromagnetic field and current distribution for RCP and LCP incident light as can be seen from Fig. 2.1 (f). This result confirms earlier theoretial predictions [8, 15] and is in agreement with the analytical model obtained from TCMT.

Introduction of Ohmic loss breaks the time reversal symmetry and considerably changes the absorption for RCP and LCP incident light that results in chiral dirchoism in absorption(CDA). Due to vastly different electromagnetic field distribution induced by the incident waves of opposite chirality, the absorption in the antennas is different ($\Delta A = A_R - A_L \neq 0$) which leads to CDT.

As can be seen from Fig. 2.1 (g) transmission of light for both polarizations is weakened compared to that without ohmic losses, however the effect is stronger for RCP light.

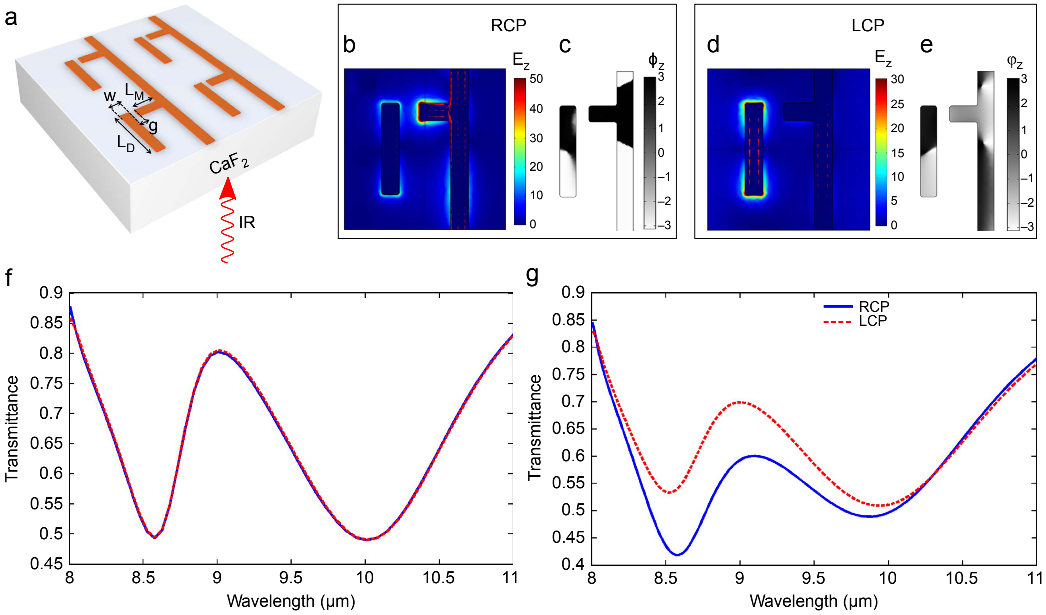

Figure 2.1: (a) Schematic of a periodic metasurface (four unit cells shown) illuminated from under the CaF_2 substrate. (b,d) Color surface: Amplitude of normal component of electric field (E_z) Arrows: inplane current distribution (c,e) phase of the normal component of electric field E_z obtained from COMSOL simulations for normally incident RCP (b,c) and LCP (d,e) light. (f,g) Transmission spectra of the metasurface for RCP (blue solid line) and LCP (red dashed line) with(g) and without(f) Ohmic losses in metal. Parameters used in simulation: $P_x = P_y = 6\mu m$, $L_m = 1\mu m$, $L_D = 3.3\mu m$, $w = 0.6\mu m$, $g = 0.4\mu m$. Frequency-dependent refractive index of gold was obtained from ref. [14], refractive index of 1.32 was used for the substrate

2.3 Experimental demonstration of circular dichroism

In order to experimentally support the COMSOL simulations and analytic theory developed earlier in the text, field distribution and transmission coefficients were measured using two complementary techniques: scattering scanning nearfield optical microscopy (s-SNOM) and atomic force microscopy(AFM). The nanoscale topographies of the two metasurface enantiomers are shown in Fig. 2.2 (a) and (b). They are fabricated on top of a mid-infrared transparent CaF2 substrate using e-beam lithography, followed by gold deposition and the lift-off. From symmetry observations illuminating a chiral structure with RCP/LCP light is equivalent to illuminating two enantiomers of it with only RCP or LCP light.

Circularly polarized light pulses from a tunable quantum cascade laser (QCL) were used to illuminate the bottom enantiomer.

The transmission spectra for RCP/LCP light is shown in Fig. 2.3 (c). They were measured across the spectral interval of $(8.5-11\mu m)$. The results demonstrate strong CDT which is pronounced around the resonant frequency $(9\mu m)$ of the monopole antenna.

For the field-scanning s-SNOM experiment, the structure was illuminated through the CaF_2 substrate by RCP light generated by a CO_2 laser at $\lambda = 9.3\mu m$. The schematics is shown in Fig. 2.3 (3). The experimental results shown in Fig. 2.3 (b,c) clearly demonstrate that near field distribution strongly depends on handedness of illuminating light for a given enantiomer[16]. The monopole antenna

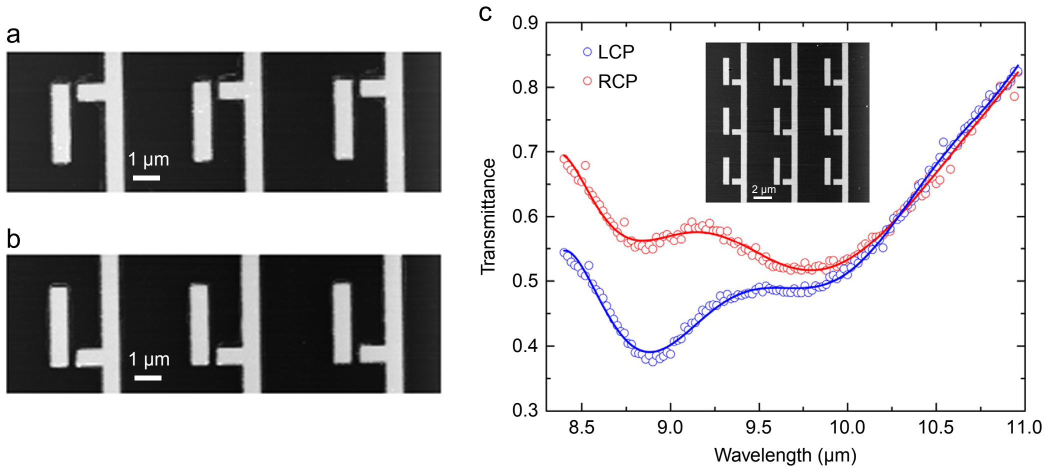

Figure 2.2: (a,b) AFM image of the enantiomers fabricated on top of CaF2 substrate. The two enantiomers(top and bottom rows) are mirror images of each other. (c) Experimental far-field transmission for the structure shown in the inset (3x3 unit cells). Circles represent the experimental points for LCP (blue) and RCP (red) incident light; solid lines are for guiding the eye.

shows strong amplitude signal only for the upper enantiomer, while the fields completely vanish at the monopole antenna for the lower enantiomer.

To show that different electromagnetic field distribution around the antennas cause different Ohmic loss in the structure, heat distribution was measured using the AFM technique. The technique was intended for nanospectroscopy of organic compounds [17, 18, 19], however it can also be used to image local heat generation in nanoantennas by observing the expansion of polyethylene film deposited on top of antennas. Since the film is transparent in the spectral region of interest, we may safely assume that all the heat is generated by ohmic dissipation in gold.

To measure the heat dissipation, a 100 nm layer of polyethylene was deposited on top of metasurface for the lower enantiomer. Polyethylene layer helps improve

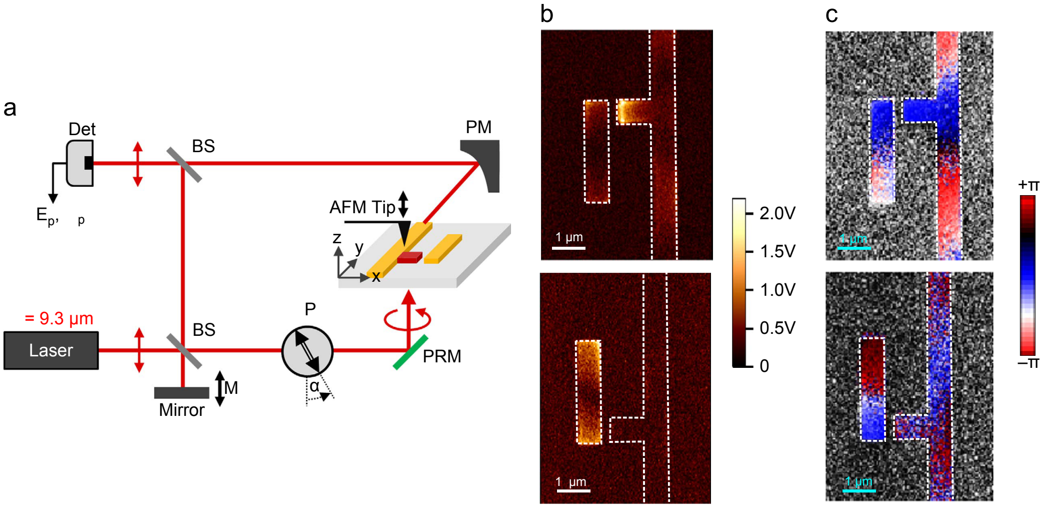

Figure 2.3: (a) Schematics of the experimental s-SNOM setup for measuring field above the chiral metasurface illuminated by RCP light . (b) Measured amplitude $|E_z|$ and (c) phase ϕ of the normal electric field E_z at $\lambda = 9.3\mu m$. White dashed lines in (b,c) outline the geometry of the structure. BS, beam splitter; Det, pseudoeheterodyne detection; P, linear polarizer; PM, parabolic mirror; PRM, infrared phase retarding mirror.

the photo expansion signal because the coefficient of linear thermal expansion of it is an order of magnitude higher than that of gold.Circularly polarized 200 ns long light pulses at $\lambda = 9.1\mu m$ from a tunable QCL were used to illuminate the sample through the CaF_2 substrate at normal incidence. Because the thermal diffusion length in polyethylene during the laser pulse is much smaller than the characteristic size of antennas, the heat map closely follows distribution of ohmic dissipation in gold.

Figure 2.4 (c) shows the experimentally measured AFM cantilever deflection amplitude at different areas of the sample. The cantilever deflection is directly proportional to temperature increase in the sample during the laser pulse. The

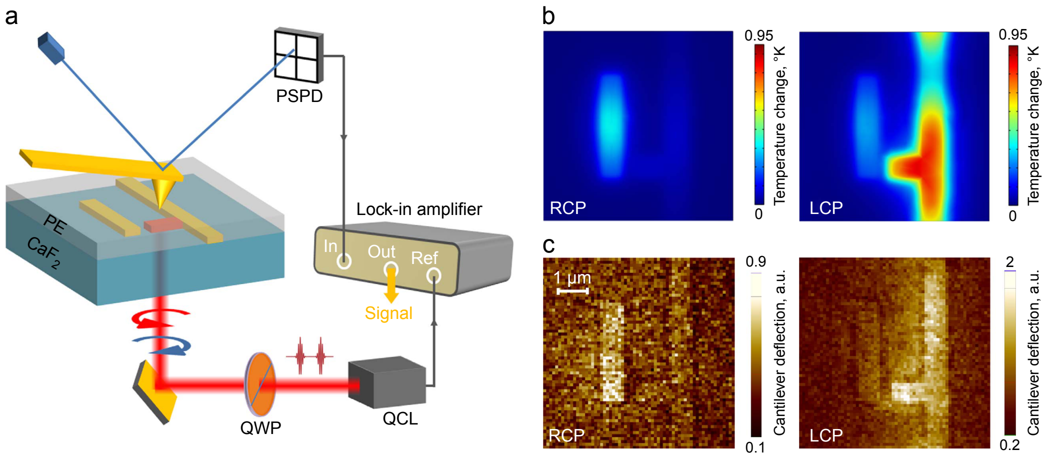

Figure 2.4: AFM-IR measurements of circularly dichroic thermal expansion of the metasurface. (a) Experimental setup. Light from a QCL passes through a quarter-wave plate (QWP) and illuminates the sample from CaF_2 substrate. Local ohmic heating of nanoantennas causes local heating and expansion of the polyethylene (PE) film and leads to cantilever deflection, which is detected by observing laser tracer beam deflection from cantilever, using positionsensitive photodetector (PSPD) and a lock-in amplifier, referenced by the QCL pulse repetition frequency. (b) COMSOL simulations of the temperature increase distribution in the polyethylene film at the end of a square QCL pulse with time duration of 200 ns tuned to $\lambda = 9.1\mu m$ mimicking the experimental conditions. (c) AFM-IR cantilever deflection on top of a PE-coated sample excited with RCP (left panel) and LCP (right panel) laser pulses at normal incidence through the CaF_2 substrate.

experimental results are in excellent agreement with COMSOL simulations shown in Fig. 2.4 (b). Magnitude and distribution of ohmic dissipation strongly depends of handedness of light that illuminates chiral 2D metasurface. As can be seen from Fig 2.4 (b,c) RCP light causes strong excitation in the dipole antenna with virtually no excitation in the monopole antenna, while for LCP light the effect is reversed.

The work in this section is based on a collaboration with coauthors in A.B.

Khanikaev, N. Arju, Z. Fan, D. Purtseladze, F. Lu, J. Lee, P. Sarriugarte, M. Schnell, R. Hillenbrand, M.A. Belkin and G. Shvets ”Experimental demonstration of the microscopic origin of circular dichroism in two-dimensional metamaterials” NATURE COMMUNICATIONS — 7:12045.

Khanikaev, Fan and Purtseladze were involved in simulations, data analysis and TCMT analytical model. Arju, Lu, Lee, Sarriugarte, Schnell, Hillenbrand and Belkin fabricated the samples and performed experimental measurements. Prof. Shvets supervised and guided the project.

3 Section C: Optical emulation of double-continuum Fano interference by circularly dichroic plasmonic metasurfaces

3.1 Introduction to Fano-resonant metasurfaces

Fano resonance is a resonant phenomena that emerges during interference between a background continous state and discrete or spectrally narrow ones. This type of interference give rise to very asymmetric line shape. Fano resonance was first introduced by Ugo Fano in his breakthrough paper [20] on ionization spectra in atoms. The idea of Fano resonances have been since applied to several ares of physics, including photonics and metamaterials[21, 22, 23, 24, 25]. The sharp and asymmetric features of Fano resonance compared to those of a conventional Lorentzian resonance allow for high electric field localization that can be used in bio sensing[26, 27] and non-linear applications[28, 29].

3.2 Double-continuum Fano interference

In this work, we investigated the interference between a single discrete state and two continuous states. Most of the recently reviewed [23, 25, 30] research on Fano resonances on optics deals with near-field coupling between two resonances: one bright and and one dark emulating the continuum and discrete atomic states. However, the original Fano paper addressed a much broader class of coupling between atomic states, including one discrete and multiple continuum states.

The key difference between the single-continuum and double-continuum cases is that the ionization probability vanishes for at least some values of energy loss of the ionizing particle in the former but not in the latter case [20]. Thus, the magnitude of Fano interference can be suppressed by the second continuum state.

In this section, we demonstrate the realization of the optical analog of double-continuum Fano (DCF) interference using a circularly dichroic (CD) plasmonic metasurface shown in Fig. 3.1 (a)

The structure possesses three egienmodes show in Fig. 3.1 (c), (d) and (e) respectively: dipolar mode along y-direction (DY), quadrupolar mode (DQ) and dipolar mode along x-direction (DX). The modes are coupled by via symmetry breaking through near field. The degree of symmetry breaking is controlled by parameter s_y which represents the displacement of the horizontal nanorod coupler (HNC) from its symmetric position.

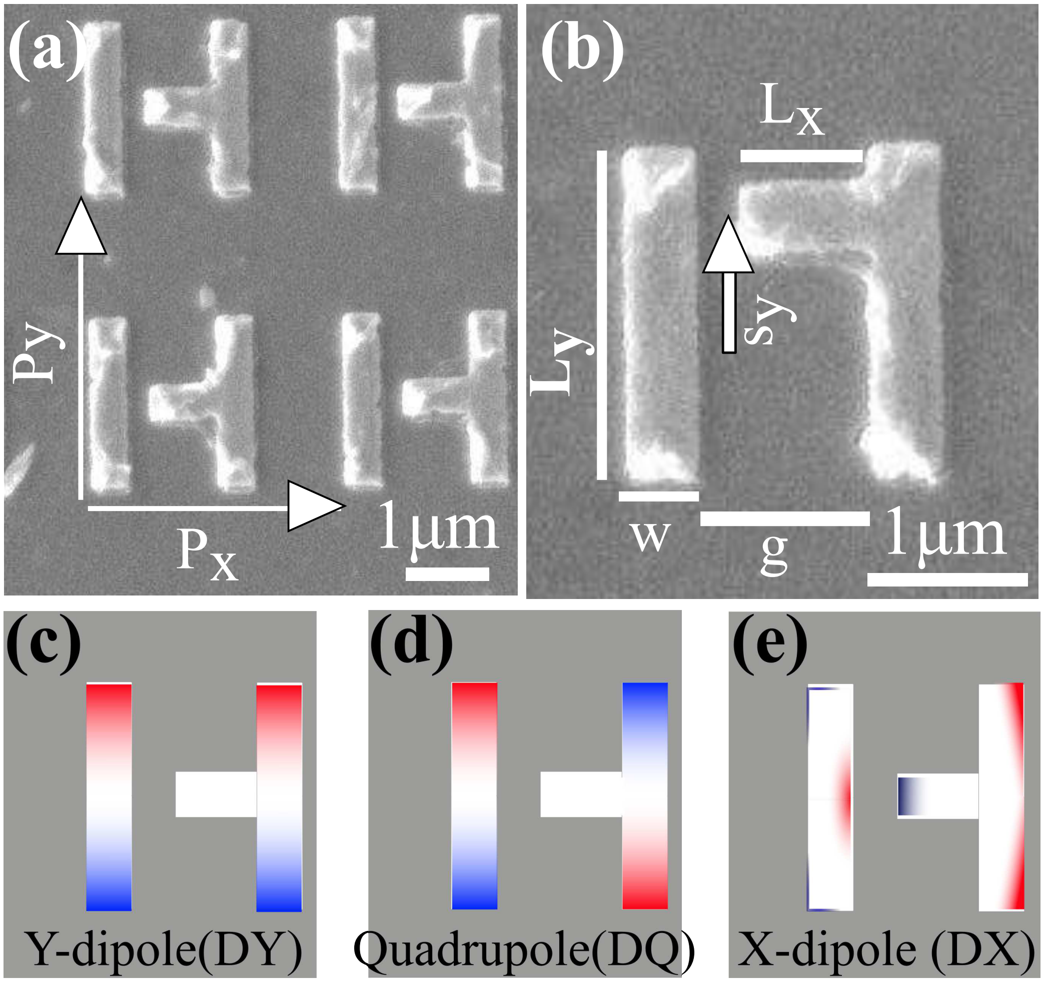

Figure 3.1: (a) Scanning electron micrograph of a fabricated DCF metasurface. (b) Geometry definitions of a unit cell $(s_y = 0.52\mu m)$. For all metasurfaces: $Px = 2.7\mu m$, $Py = 3.15\mu m$, $w = 0.36\mu m$, $Lx = 0.92\mu m$, $Ly = 1.8\mu m$, and $g = 0.66\mu m$. (d-f): Charge distributions of the three unperturbed eigenmodes of the symmetric $(s_y = 0)$ metasurface. (d) and (f): bright DY(dipolar y) and DX(dipolar x), (e): dark DQ (quadrupolar).

Experimental measurements of Fano-shaped polarized reflectivity spectra $R_x(\lambda)$ and $R_y(\lambda)$ shown in Fig. 3.2(a,b) reveal a new optical phenomenon of continuum state competition in asymmetric photonic structures: the presence of the second (e.g., y—polarized) continuum state can significantly affect the strength of the Fano interference of the dark state with the first (e.g., x–polarized) continuum state. Unlike the plasmonic phenomenon [31] of the Fano feature reduction by non-radiative (Ohmic) losses, the continuum state competition directly emulates the atomic systems [20] where the non-radiative decay rate of the discrete state is naturally negligible.

A family of gold metasurfaces shown in Fig. 3.2 with different symmetry-breaking parameters s_y were fabricated on CaF_2 substrates using electron beam lithography. The lowest plasmonic resonances of the metasurfaces shown in Fig. 3.2 are classified as one dark quadrupolar (DQ) and two bright dipolar (DX and DY) plasmonic modes that are radiatively coupled to incident linearly polarized light in the x– and y–directions, respectively, giving rise to two quasi-continua of electromagnetic states. The finite displacement s_y of the HNC that perturbs the DQ mode is used to control the coupling between the modes. Polarized reflection coefficients were measured using Fourier transform infrared microspectroscopy. The $R_{yy}(\lambda)$ and $R_{xx}(\lambda)$ spectra shown in Fig. 3.2(a) reveal broad reflectivity peaks inside the shaded ($4.5\mu m < \lambda < 6\mu m$) spectral window, corresponding to the bright DY and DX resonances, respectively. We concentrate on the $6\mu m < \lambda_{DQ}(s_y) < 8\mu m$ spectral range containing the dark DQ mode.

By studying the spectra several observations can be made. We conclude from Fig. 3.2 that the relative coupling strengths $\kappa_{XQ}(s_y)$ (between DQ and DX) and $\kappa_{YQ}(s_y)$ (between DQ and DY) vary widely with s_y. This conjecture follows from the very different manifestations of Fano resonance in R_{xx} and R_{yy} spectra. Specifically, for small values of $s_y < L_y/4$, the Fano feature in the x–polarization becomes strongly pronounced while it is barely noticeable in y–polarization (e.g., $s_y = 0.52\mu m$). The opposite is true for large values of s_y: the Fano feature in $R_{yy}(\lambda)$ is much stronger than in $R_{xx}(\lambda)$ for $s_y > L_y/2$ (e.g., $s_y = 1.12\mu m$).

The magnitude of the Fano feature in x—polarization is non-monotonic in s_y. The peak value of R_{xx} (dotted line) plotted in Fig. 3.2(b) increases with s_y, reaches the maximum at $s_y = 0.52\mu m$, and then decreases.The decrease of the Fano feature for large values of s_y is unexpected because the coupling coefficient $\kappa_{XQ}(s_y)$ continues to increase with s_y. The observed decrease is the direct experimental evidence of continuum state competition in DCF originally predicted by Fano [20] for atomic systems. Specifically, the linewidth of the radiatively-broadened Fano resonance increases (and the corresponding quality factor decreases faster with s_y than the coupling coefficient $\kappa_{XQ}(s_y)$, thereby suppressing the Fano feature in R_xx reflectivity spectrum.

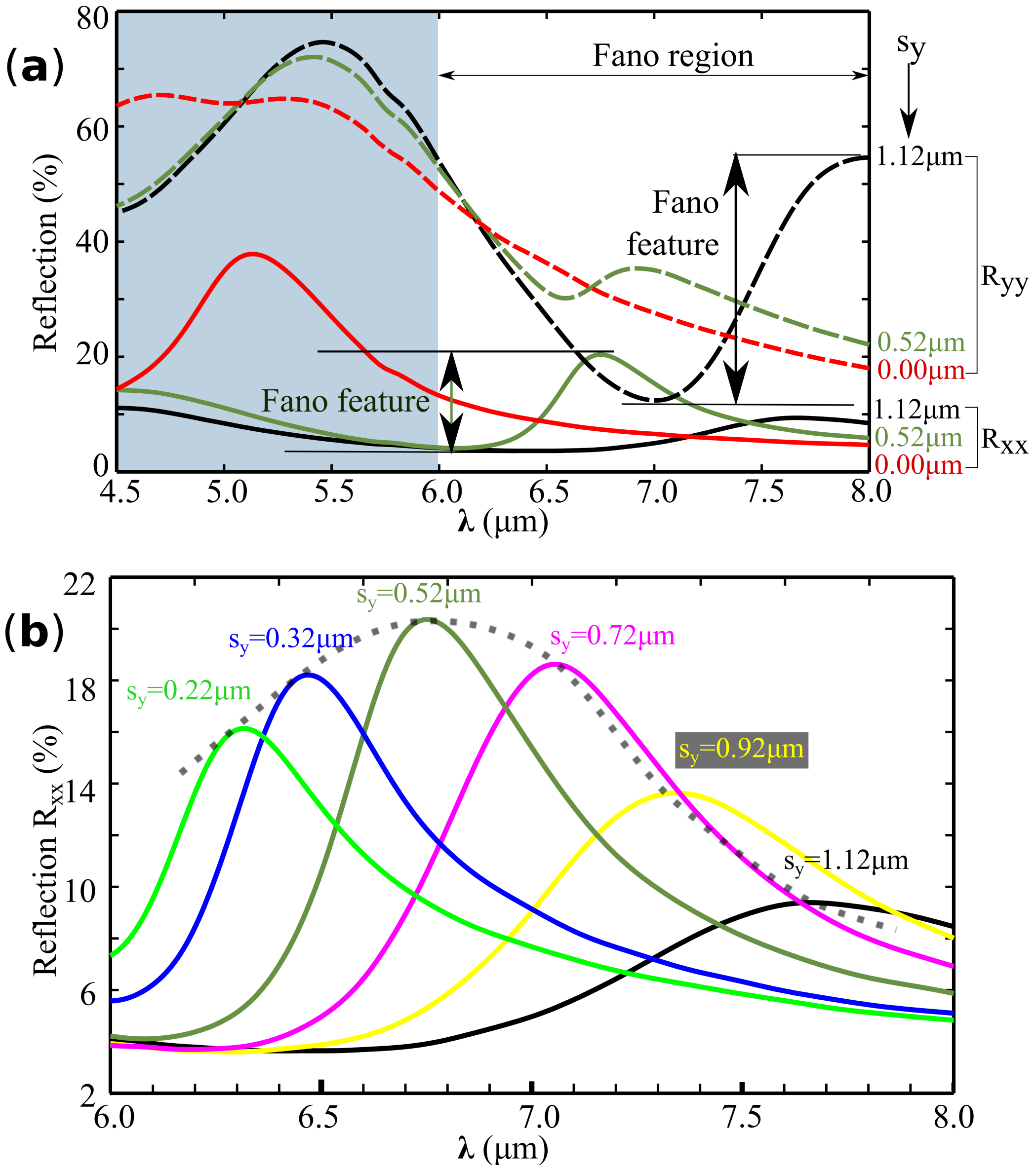

Figure 3.2: (a) Measured reflectivity spectra R_{xx} (solid lines) and R_{yy} (dashed lines). Fano feature in R_{yy} is larger than in R_{xx} for $s_y = 1.12\mu m$ (black line); opposite is true for $s_y = 0.52\mu m$ (green line). Fano features are absent for $s_y = 0$ (red lines). (b) Zoomed-in R_{xx} spectra for $0.22\mu m < s_y < 1.22\mu m$ Dotted line: non-monotonic behavior of the Fano feature with s_y interpreted as the competition between x and y polarized continua.

3.3 Analytical model describing DCF interference

To explain these experimental results and to explore the possibility of circularly dichroic optical field concentration, in what follows we develop a simple analytic model of optical DCF. The interaction of light with the three modes (two quasi-continuum and one discrete) of the metasurface is described by the following equations based on TCMT:

$$
\begin{aligned}
\frac{dD_Y}{dt} &= i\omega_X D_Y + i\kappa_{XY} D_X + \alpha_Y E_y \\
\frac{dQ}{dt} &= i\omega_Q Q + i\kappa_{XQ} D_X \\
\frac{dD_X}{dt} &= i\omega_X D_X + i\kappa_{XY} D_Y + i\kappa_{XQ} Q + \alpha_x E_x
\end{aligned}
\tag{3.1}
$$

where D_X, D_Y , and Q are the mode amplitudes, and $\alpha_{x,y}$ are the radiative coupling coefficients of the bright resonances to the x,y–polarized incident field with amplitudes $E_{x,y}$ respectively.

The three modes are characterized by their complex-valued unperturbed eigenfrequencies $\omega_{X,Y,Q} = \omega^0_{X,Y,Q} - i\tau^{-1}_{X,Y,Q}$ where $\omega^0_{X,Y,Q}$ and $\tau_{X,Y,Q}$ are resonant frequencies and mode lifetimes respectively.

The κ_{YQ} near-field coupling coefficient has been neglected in comparison with its $\kappa_{XQ}(s_y)$ and $\kappa_{XY}(s_y)$ components for small value of s_y. Qualitatively, the coefficients are proportional to the overlap integral $E_i \bullet E_j$ of electric field produced by modes (i,j) inside the region occupied by the HNC. In can be observed from Fig. 3.1(c-e) that (a) E_x is the largest electric field component for all three modes in the said region of space, and (b) $E_x = 0$ at y = 0 for the DQ and DY modes. Therefore, it is expected that κ_{XQ}, κ_{XY} will be proportional to s_y, but κ_{YQ} will be proportional to s^2 and can be neglected for small (less than $L_y/4$) values of s_y. From energy conservation law, total decay rate is calculated from radiatave loss and Ohmic loss [30, 32]: $1/\tau_{X,Y} = \alpha^2_{X,Y} + 1/\tau_O hm$

Solving Eq. 3.1 in the vicinity of the dark resonance under the assumption of small-coupling ($| \kappa_{XY} |, | \kappa_{KQ} | \ll | \omega^0_Q - \omega^0_{X,Y} |$) using the expressions for the complex-valued reflection amplitudes [30] $r_{xx,yy} = \alpha^*_{x,y} D_{X,Y}/E_{x,y}$ we obtain:

$$\begin{aligned} r_{xx} &= \frac{\alpha_x^2}{\omega - \omega_X} + \frac{\alpha_x^2 \gamma_{XY}^2}{\omega - \omega_Y} + \frac{\alpha_x^2 \gamma_{XQ}^2}{\omega - \omega_Q^{(r)}} \\ r_{yy} &= \frac{\alpha_y^2}{\omega - \omega_Y} + \frac{\alpha_x^2 \gamma_{XY}^2}{\omega - \omega_X} + \frac{\alpha_x^2 \gamma_{YQ}^2}{\omega - \omega_Q^{(r)}} \end{aligned} \tag{3.2}$$

where the normalized coupling coefficients $\gamma_{i,j}$ between the modes are given by:

$$\begin{aligned} \gamma_{XY} &= \kappa_{XY}/(\omega_X - \omega_Y) \\ \gamma_{XQ} &= \kappa_{XQ}/(\omega_X - \omega_Q) \\ \gamma_{YQ} &= \gamma_{XY}\gamma_{XQ} \end{aligned} \tag{3.3}$$

The renormalized/red-shifted frequency $\omega_Q^{(r)}$ and the radiatively reduced lifetime $\tau_Q^{(r)}$ of the DQ mode are approximated as:

$$
\begin{aligned}
\omega_Q^{(r)} &\approx \omega_Q^0 - \frac{\kappa_{XQ}^2}{\omega_X - \omega_Q^0} - \frac{\kappa_{XY}^2 \kappa_{XQ}^2}{(\omega_X - \omega_Q^0)^2 (\omega_Y - \omega_Q^0)} \\
\frac{1}{\tau_Q^{(r)}} &\approx \frac{1}{\tau_Q^{Ohm}} + \kappa_{XQ}^2 \frac{\alpha_x^2}{(\omega_X - \omega_Q^0)^2} + \kappa_{XY}^2 \kappa_{XQ}^2 \times \\
&\frac{\alpha_y^2 (\omega_X - \omega_Q^0)^2 + 2\alpha_x^2 (\omega_X - \omega_Q^0)(\omega_Y - \omega_Q^0)}{(\omega_X - \omega_Q^0)^4 (\omega_Y - \omega_Q^0)^2}
\end{aligned}
\tag{3.4}
$$

The key features of the experimentally measured $R_{xx,yy} = \mid r_{xx,yy} \mid^2$ reflectivity spectra can now be understood by examining the dependence of the Fano features magnitude $r_{xx,yy}^{Fano}$ on s_y. It is given by the third terms in the equations of Eq. (3.2) evaluated at $\omega = \omega_Q^{(r)}$:

$$
\begin{aligned}
r_{xx}^{Fano} &\propto \frac{\alpha_X^2 s_y^2}{1/\tau_Q^{Ohm} + \beta s_y^2 + \delta s_y^4} \\
r_{yy}^{Fano} &\propto \frac{\alpha_Y^2 s_y^4}{1/\tau_Q^{Ohm} + \beta s_y^2 + \delta s_y^4}
\end{aligned}
\tag{3.5}
$$

where coefficients β and δ can be found from Eq. (3.4) We observe that the decay rate of the DCF resonance given by the denominators of Eq.(3.5) can be broken up into three contributions: (a) the ohmic (non-radiative) contribution, (b) the contribution proportional to s_y^2 corresponding to the radiative decay into the x—polarized continuum, and (c) the contribution proportional to s_y^4 corresponding to the radiative decay into the y-polarized continuum. Depending on the relative dominance of these three mechanisms controlled by s_y, the three respective coupling regimes can be identified as (i) weak coupling regime $s_y < L_y/4$), (ii) intermediate coupling regime $(L_y/4 < s_y < L_y/2)$, and (iii) strong coupling regime $s_y \sim L_y$. The transition from weak to strong coupling regimes with increasing s_y

explains the decrease of the quality factor of the Fano resonance with s_y evident from Fig. 3.2 (b). The experimentally estimated quality-factors of the DQ mode drop from its Ohmic loss limited value of Q = 13 to Q = 7 (strong y–polarized radiative loss) as s_y increases from $0.22\mu m$ to $1.12\mu m$.

One of the attractions of Fano resonant metasurfaces is strong optical field enhancement due to the excitation of dark plasmonic resonances. Controlled by the geometry, those can be utilized for sensing and nonlinear applications. As we demonstrate below, optical field concentration can also be controlled through interference by engineering a general elliptic polarization state of the incident light. This effect can induce CD in transmission and absorption.

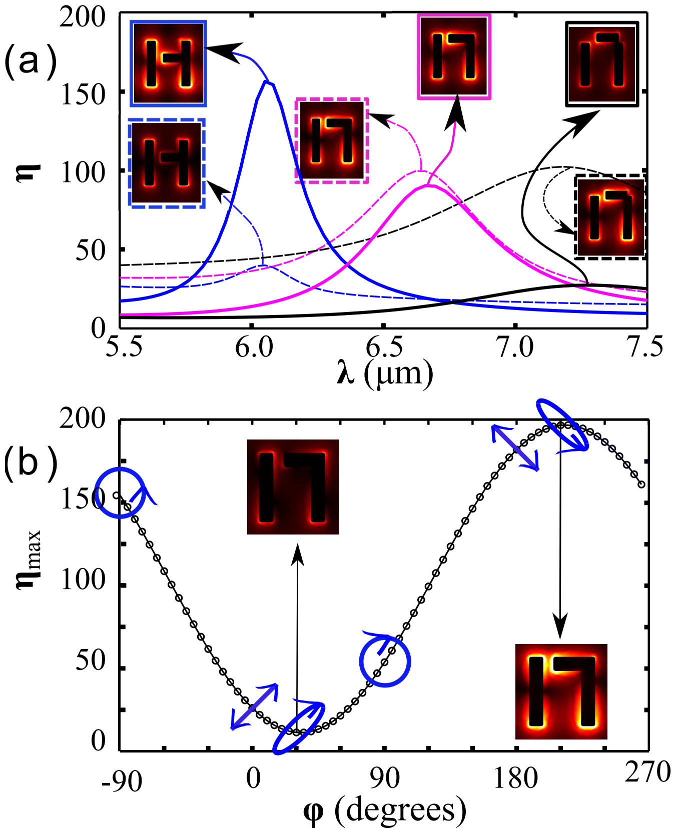

Figure 3.3: COMSOL simulations of the optical intensity enhancement $\eta = E^2/E_0^2$ averaged overall (except metal-substrate) metal interfaces in plasmonic DCF metasurfaces. (a) η for x–polarized (solid) and y–polarized (dashed lines) incident light for weak-coupled ($s_y = 0.32\mu m$), intermediately-coupled ($s_y = 0.72\mu m$), and strongly-coupled ($s_y = 1.14\mu m$) regimes. Insets: near field profiles. (b) The dependence of η_{max} on the incident light chirality parametrized by the phase shift ϕ for the $s_y = 0.52\mu m$ metasurface. Insets: near-field intensities for $\phi = \pi/6$ (left) and $= (7/6)\pi$ (right). Closed directional loops indicate the polarization state of incident light as a function of phase parameter ϕ.

To calculate the amplitude Q of the dark resonance in the proximity of the DQ mode in response to the incident elliptically polarized light with complex-valued amplitudes $(E_x, E_y) = (1/\sqrt{2})E_0(1, exp(i\phi))$ where ϕ is the relative phase between the x– and y– polarizations. At the Fano resonance, the amplitude of the DQ mode is expressed from Eq. (3.1) as
$Q = E_0(q_{xx} + exp(i\phi)q_{yy})/(\omega - \omega_Q^{(r)})$ where

$$\begin{aligned} q_{xx} &= \frac{\alpha_x \kappa_{XQ}(s_y)}{\omega_X - \omega_Q} \\ q_{yy} &= \frac{\alpha_y \kappa_{XQ}(s_y)\kappa_{XY}(s_y)}{(\omega_X - \omega_Q)(\omega_Y - \omega_Q)} \end{aligned} \tag{3.6}$$

Because of the different scaling of q_{xx} and q_{yy} with s_y, in case of weak (strong) coupling regime the strongest field enhancement is achieved for the x(y) polarized light. This result is confirmed by COMSOL simulations of the optical intensity enhancement averaged over the entire surface $\eta = E^2/E_0^2$ that is shown in Fig. 3.3(a).

The resulting CD is the consequence of the finite phase difference $\Delta\phi = arg(q_{xx}/q_{yy})$ between q_{xx} and q_{yy}: the field enhancement is maximized (minimized) for ($\phi_{max} = \Delta\phi$) ($\phi_{min} = \Delta\phi + \pi$) due to the constructive (destructive) interference between the two excitation pathways. From symmetry observations it is evident that transformation ($s_y \to -s_y$) switches between two opposite enantiomers of the same chiral structure.

These qualitative results are confirmed by COMSOL simulations carried out for the $s_y = 0.52\mu m$ structure chosen because $\mid q_{xx} \mid \approx \mid q_{yy} \mid$ according to Fig.

3.3(b). The peak enhancement factor $\eta_m ax$ plotted in Fig. 3.3(b) reveals strong chiral dichroism. The ratio of the highest $\phi = (7/6)\pi$ to lowest $\phi = \pi/6$ near-field intensities is around 20, and the enhancement ratio for RCP light $\phi = -\pi/2$ is three times higher than for the LCP light $\phi = \pi/2$.

It was demonstrated that a quantum mechanical phenomenon of double continuum Fano (DCF) interference can be classically emulated using an asymmetric plasmonic metasurface. The relative coupling strength between the discrete and two continuum states, distinguished from each other by their polarization, were experimentally varied by changing the degree of symmetry breaking of the metasurface. The phenomenon of continuum state competition, by which one of the continuum states suppresses the Fano resonance for the orthogonal light polarization, was observed and analytically explained.

The work in this section is based on a collaboration with coauthors in Nihal Arju, Tzuhsuan Ma, Alexander Khanikaev, David Purtseladze, and Gennady Shvets ”Optical emulation of double-continuum Fano interference by circularly dichroic plasmonic metasurfaces”, Nature Communications 7, 12045 (2016).

Khanikaev, Purtseladze and Ma were involved in data analysis and TCMT analytical model. Arju fabricated the samples and performed experimental measurements. Prof. Shvets supervised and guided the project.

4 Section C: One-way-leaky waveguides based on nonreciprocal Fano-resonant metasurfaces

4.1 Introduction

Non reciprocal devices [3] play a crucial role in photonics application across the electromagnetic spectrum from microwave [4] to optical frequencies [33]. These devices force the electromagnetic waves behave differently depending on their direction of propagation. For both mircowave and optical applications, nonreciprocal devices are utilizing symmetry breaking provided by transparent ferrites [34] with gyrotropic forms of permittivity and permeability. The off-diagonal elements of the permeability tensor that characterizes the strength of magneto optical effects can be large in the microwave range, however this is not the case for optical frequencies. This restriction results in very large dimensions of nonreciprocal elements which limits their application in modern photonic circuitry. These limitations have also attracted a tremendous interest in exploring the design capabilities of structured nonreciprocal materials, including magnetic photonic crystals and plasmonic metamaterials and metasurfaces incorporating ferrites [35, 36, 37]. It has been shown that by utilizing resonances in photonic crystal cavities, nanoparticles, and plasmonic metasurfaces, the nonreciprocal effects can be dramatically enhanced. Indeed, it is known that enhanced density of photonic states within the magneto-optical materials boosts light-matter interactions and enhances magneto-optical effect.

Recently, it has been demonstrated that in structures with complex geometries, metasurfaces hosting highly localized subradiant modes, one can exploit symmetries of the modes to achieve intriguing nonreciprocal effects of a new type, such as one-way Fano-resonances and one-way slow light [5]. In this section we will apply these concepts and propose a microwave nonreciprocal meta-waveguide whose subwavelength patterning is designed to benefit from i) the localized character of subradiant (dark) modes and their interaction with the modes of a conventional two dimension waveguide that results in strong hybridization of modes. The structure is then used to build a meta-channel waveguide which supports unique nonreciprocal one-way leaky modes; such channel modes are guided in one direction without loss while propagation in the opposite direction results in energy leaking into the surrounding cladding.

4.2 Realization of One-way-leaky waveguide based on nonreciprocal FRAMMs

The geometry of the structure is shown in Fig. 4.1(a). Its unit cell consists of a pair of clamps facing each other in a way that a split ring resonator (SRR) metamolecule with two gaps is formed. The metamolecules rest on the layer of ferrite magnetized in y—direction and placed on top of a perfectly conducting metallic back-plate.

The ferrite with back-plate represents a waveguide whose modes, in the absence of the metamolecules, can be conventionally classified as TE (TM) modes with their electric (magnetic field) components being transverse to the propagation direction. The gyrotropic response of the ferrite magnetized in the y— direction is described by the following permeability tensor:

$$\mu = \begin{pmatrix} \mu_{xx} & 0 & i\kappa \\ 0 & \mu_{yy} & 0 \\ -i\kappa & 0 & \mu_{zz} \end{pmatrix} \tag{4.1}$$

When the ferrite is magnetized, for most propagation directions, namely when there is magnetization component along propagation (the Faraday geometry), these modes couple giving rise to mode conversion. However, such conversion is extremely inefficient, unless the phase matching condition is met. However introduction of the metamolecule on top of ferrite induces artificial periodic conditions that results in folding of modes. Moreover, the metamolecule itself hosts a dark magnetic dipole (MD) resonanse in the spectral region of interest. Both MD and TE posses a component of magnetic field in the z— direction that results in mode conversion. The avoided crossing between TE and MD is clearly visible in Fig. 4.1 (b) and (c). Conversely, the folded TM mode does not interact with either TE or MD in case of non-magnetized ferrite. All numerical simulations were carried out with the following ferrite parameters: permeability $\mu_{xx} = \mu_{yy} = \mu_{zz} = 2.25$, $\kappa = 0$(unmagnetized), $\kappa = 1.45$(magnetized), permettivity $\varepsilon = 12.9$.

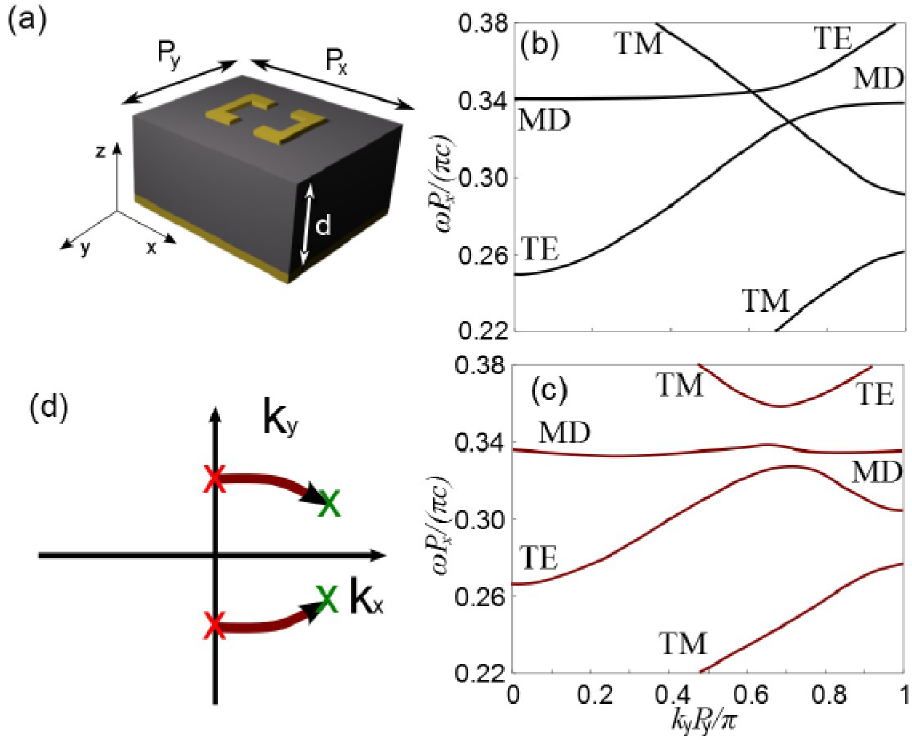

Figure 4.1: (a) Unit cell design. Dimensions $P_x = 2cm$,$P_y = 1.7cm$, ferrite width $H = 9.17mm$, ferrite permittivity $\varepsilon = 12.9$ (b) Dispersion without external magnetization $\kappa = 0$, interaction between TE and MD opens the gap, while TM does not interact with either TE or MD (c) Dispersion with external magnetization $\kappa = 1.45$ All three modes (TE,TM and MD) interact which results in opening of two gaps (d) Schematic showing how the intersection of TE and TM modes shifts as we introduce finite external magnetization κ. Dispersion in (b) and (c) is plotted for propagation along y—direction (i.e. $k_x = 0$)

The band diagram for the structure in question is shown in Fig 4.1 (b) and (c). The two paths of mode interaction stem from symmetry breaking: time-reversal and spacial inversion. In case of violation of time-reversal symmetry, we magnetize the ferrite ($\kappa = 1.45$) and observe waves that propagate along y— direction. This results in avoided crossing (Fig. 4.1 (c)) between TE, TM and MD. This avoided crossing creates a slow light region where guided mode has a low group velocity and high density of states. When the ferrite is unmagnetized and waves propagate along y— direction (i.e. $k_x = 0$) the modes do not interact as it can be seen from Fig. 4.1 (b): the folded TM modes crosses both TE and MD modes.

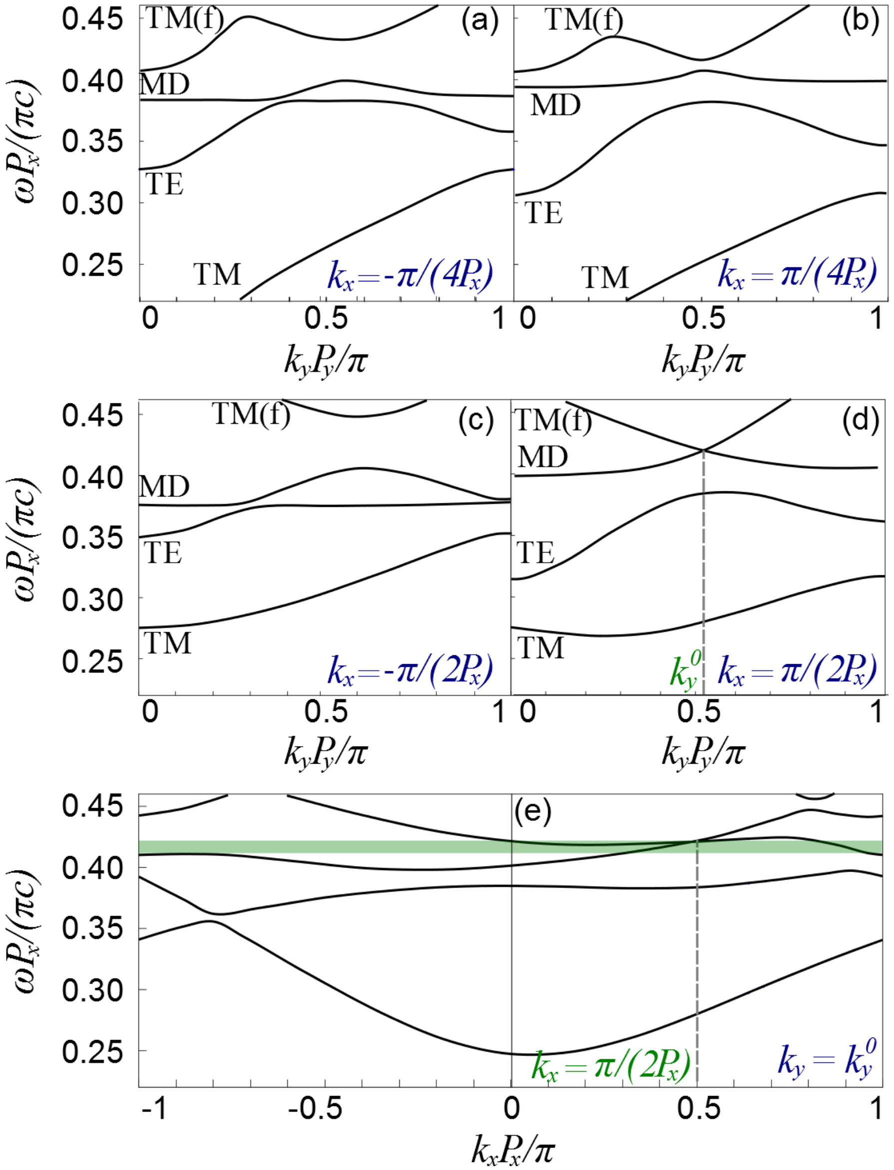

Figure 4.2: (a,b,c,d) band diagrams spanning whole Bruillion zone in y— direction for different values of k_x, (c,d) Band diagrams exhibit strong non-reciprocity: for opposite values of k_x (c) shows a band gap while (d) does not.(e) Band diagram showing dispersion for a fixed value of $k_y^0 = 89.3m^{-1}$ spanning all values of k_x

It is worth emphasizing that the band diagram does exhibits strong nonreciprocity, however this non-reciprocity occurs in x—direction. As can be seen from Fig. 4.2 (a,b,c,d) the band diagrams are quite different for different values of k_x and k_y, the graphs represent different vertical cut planes in the $(k_x, k_y, f^{(n)})$ space where $f^{(n)} = \omega P_x/(\pi c)$ is normalized dimensionless frequency. The one-way non-reciprocal region emerges for certain values of k_x, k_y and geometric parameters of the structure. By choosing $k_x^0 = \pi/(2P_x)$ and tuning the parameters of the structure we were able to obtain a fairly wide ($\Delta\omega/\omega = 0.03$) bangdap for negative values of $k_x = -k_x^0$ simultaneously closing the gap for positive values of $k_x = k_x^0$. The gap is marked with green shaded region, shown in Fig. 4.2(e).

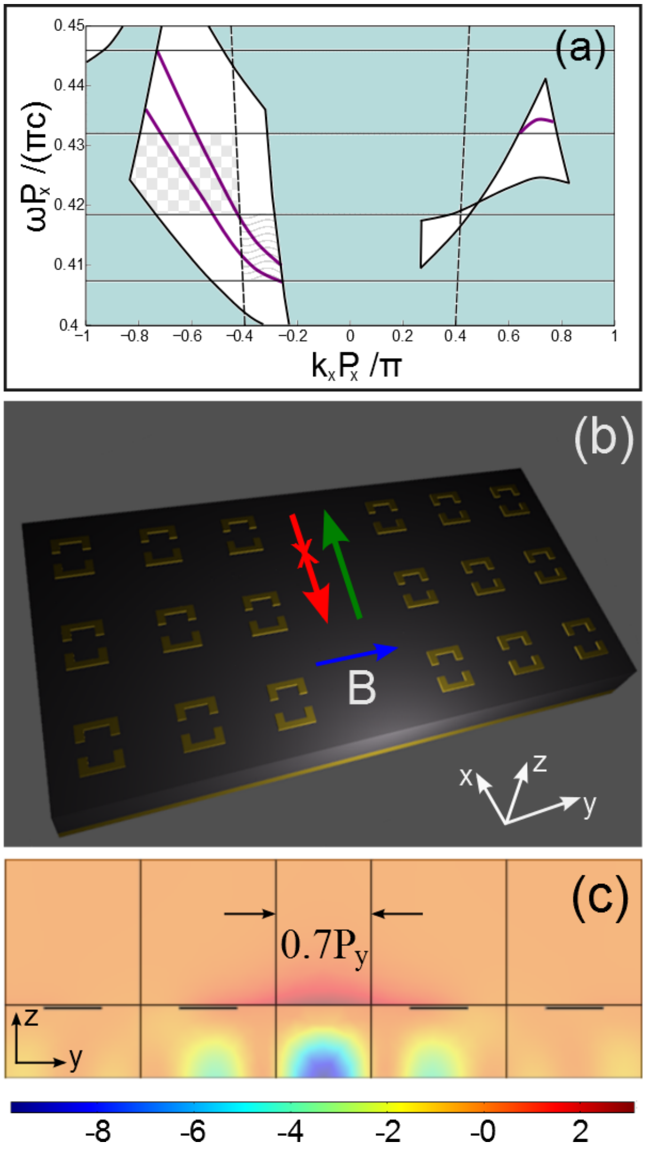

Figure 4.3: (a)Band diagram obtained by superposition of band diagrams for all possible values of k_y shows one-way band gap and edgemodes(purple line) within the gap. (c) Schematics of the waveguide, the channel represents the waveguide while clamps act as cladding (d) Energy $\mid E \mid^2$ profile for one of the edge modes shows high localization within three unit cells from the channel.

We utilized non-reciprocal behavior of this structure to design a one-way waveguide. The schematics of this waveguide is shown in Fig. 4.3 (b). The clamps act as a cladding for the guiding channel in the middle. From the band diagram (Fig 4.3 (a)) obtained from superimposing band diagrams for all possible values of k_y it is evident that inside the channel waves propagating in the negative x—direction do so unhindered, while waves propagating in the positive x—direction will leak into the cladding and eventually decay. To verify this statement, COMSOL driven simulation for a super cell shown in Fig. 4.4 (a,b)was carried out. The modes were excited by two current sheets indicated by shaded regions in the middle of the channel. The simulation results show time-average power flow along x— direction. Strong non-reciprocal behavior is observed: waves propagate without loss in negative x— direction($k_x < 0$), but leak into the cladding and decay if direction is reversed($k_x > 0$).

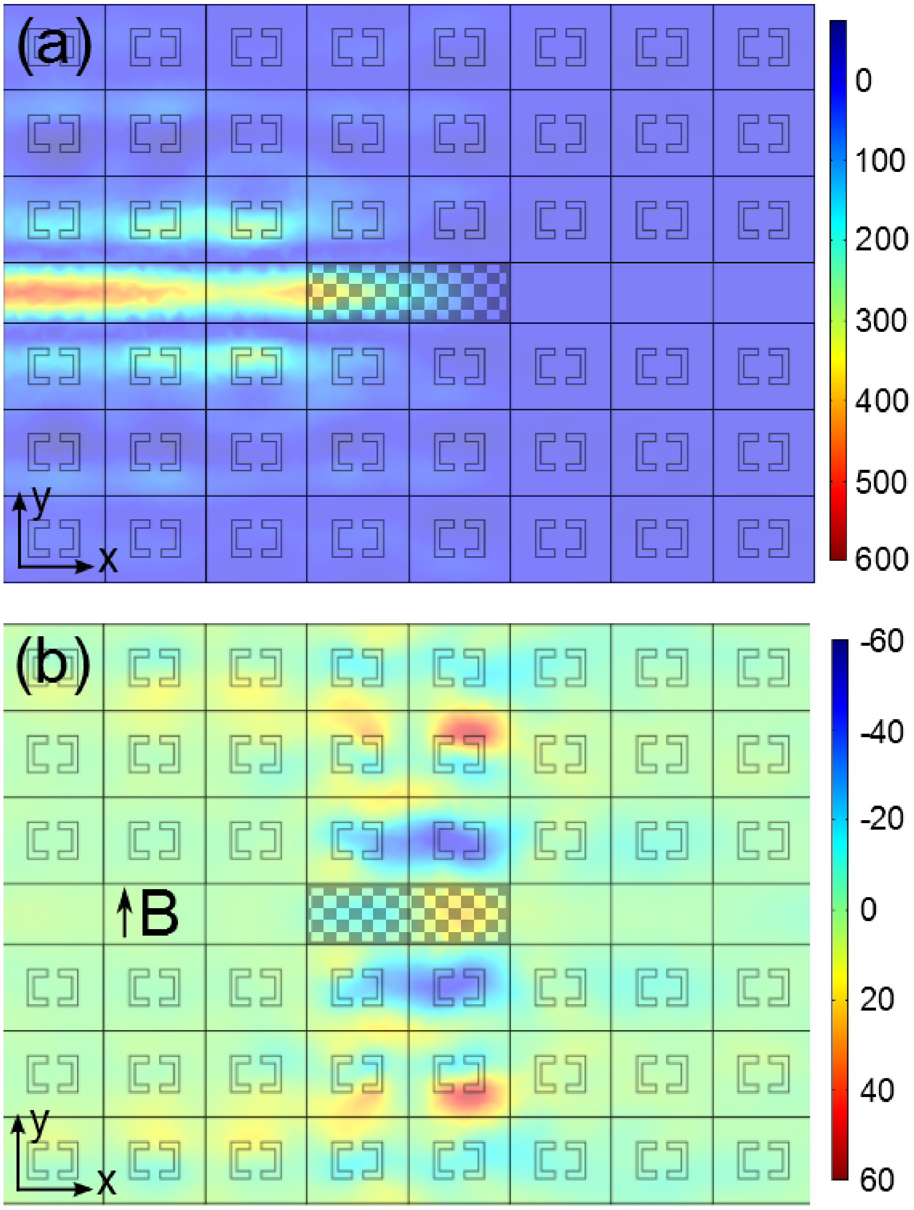

Figure 4.4: Average power flow along x— direction for waves launched left (a) and right (b). Waves were excited by two current sheets(shaded regions). Waves launched right leak into the cladding and decay within three unit cells from the launch point, while those launched left propagate without significant losses.

5 Section D:One-way Klein tunneling

5.1 Introduction

Klein tunneling, the unimpeded penetration of particles through potential barriers, is a fascinating phenomenon first encountered in relativistic quantum electrodynamics of highenergy fermions [38]. In nonrelativistic quantum mechanics, tunneling of a massive particle into a potential barrier is observed with exponential damping. Klein's breakthrough paper showed that if the potential barrier is of the order of the electron energy-mass ($U \sim me^2$), the barrier is nearly transparent. Moreover, as the potential barrier approaches infinity, electron transmission approaches unity. Recently, a prediction of this exotic chiral transport was experimentally confirmed [39, 40] in junctions of graphene, a layer of carbon atoms arranged in a honeycomb lattice [40], owing to its quasi-relativistic carrier dynamics described by the effective massless Dirac equation [41, 42, 43]. Optical analogue of this two-dimensional (2D) crystal, photonic graphene [44, 45] holds enormous potential for applications in photonic circuits [46, 47]. The degeneracies with crossed linear Dirac-like dispersion in honeycomb crystals are protected by parity (P) and time-reversal (TR) symmetries (PT). In photonic lattices such Dirac cones have to appear in pairs, unless time-reversal symmetry is broken. For this reason, the photonic graphene exhibits two pairs of Dirac cones in its Brillouin zone.

5.2 One-way Klein tunneling

We proposed coupling valley and orbital degrees of freedom by reducing both P and TR symmetries,which results in nonreciprocity and uneven opening of band gaps at K and K points, and emergence of one-way Dirac cone at one of the valleys. Such dispersion ensures one way photonic transport in the structure that leads to non-reciprocal one way Klein tunneling. The waves coupled to one valley propagate unimpeded, while transmission through the other valley falls in a band gap and is blocked or demonstrates oscillatory behavior at the edges of the gap. This behavior is caused by parabolic dispersion of the valley in the vicinity of the band gap.

For numerical COMSOL simulation, an array of high-index ferromagnetic rods laid out in a honeycomb lattice was used to emulate graphene , as illustrated in Fig. 5.1(a) The bipartite unit cell consists of two cylinders with radii r_A and r_B. The lattice constant of a triangular lattice is denoted by a. The permittivity of the rods ε is a scalar, whereas the gyrotropic response of the ferromagnetic material induced by a static magnetic field B directed along z-axis near the ferromagnetic resonance is described by the magnetic permeability tensor:

$$\mu = \begin{pmatrix} \mu & i\kappa & 0 \\ -i\kappa & \mu & 0 \\ 0 & 0 & \mu_{zz} \end{pmatrix} \tag{5.1}$$

Two types of symmetry breaking can be introduced to this system, resulting in two distinct quantum-Hall-like [48] and valley-Hall topological phases [49]. In the photonic graphene, the valley-Hall phase is induced by the reduction of the sublattice symmetry due to the dimerization of cylinders A and B, i.e., by making the radii unequal. The quantum-Hall-like phase is achieved by breaking of TR symmetry due to magnetization.

The effective Hamiltonian describing both states can be obtained from Maxwell's equations using the plane wave expansion method[48]. After taking into account the valley degree of freedom, the effective Hamiltonian assumes the form:

$$\hat{H} = \begin{pmatrix} \hat{H}_K + (m_{\mathrm{T}} - m_{\mathrm{I}})\hat{\sigma}_z & 0 \\ 0 & \hat{H}_{K'} - (m_{\mathrm{T}} + m_{\mathrm{I}})\hat{\sigma}_z, \end{pmatrix} \tag{5.2}$$

where $\hat{H}_{K(K')} = V\left(\pm\delta k_x\hat{\sigma}_x + \delta k_y\hat{\sigma}_y\right)$ are Dirac Hamiltonians, and two mass terms originate from different symmetry reductions. Here, we assume negligible intervalley scattering. If we artificially tune the structure and make the masses equal $m_I = m_T$, the bandgap is closed at K while doubled at K'. In K' valley, the dispersion exhibits an energy gap between two bands

$$\Omega_{\pm}(\delta k) = \pm\sqrt{v^2(\delta k_x^2 + \delta k_y^2) + m^2}\,, \tag{5.3}$$

where the mass $m = m_I + m_T$. For small δk the dependence $\Omega_{\pm}(\delta k)$ in Eq. (5.3) is quadratic.

We consider a one dimensional structure that consists of three regions $1/2/1$, where domains 1 and 2 are characterized by total masses $m_{1,2}$ and homogeneous potentials $u_{1,2}$. We assume the case of normal incidence $\delta k_y = 0$ of the propagating wave ($|\Omega| > m_1$) from the region 1 along the x axis onto the potential obstacle of the amplitude $(u_2 - u_1)$ in the domain 2, which is infinitely long in y direction and has a finite width L. We solve for the wavefunctions in each of the regions with the respective Hamiltonians and then match them. The resultant transmission coefficient:

$$T = \frac{4s_1^2|s_2|^2}{\left|2s_1s_2\cos\left(\delta k_{2x}L\right) - i[s_1^2 + s_2^2]\sin\left(\delta k_{2x}L\right)\right|^2}, \tag{5.4}$$

where $s_{1,2} = \sqrt{(\Omega - u_{1,2})^2 - m_{1,2}^2}/(\Omega - u_{1,2} - m_{1,2})$, $\delta k_{2x} = \sqrt{(\Omega - u_2)^2 - m_2^2}/V$. Taking $m_1 = u_1 = 0$ and other fitting parameters of the computed crystal supercell, analytically retrieved transmission is plotted in Fig. 5.3(b) with a green dashed line. For the normal incidence, the well is perfectly transparent in K valley, which is directly related to the Klein paradox and the conservation of pseudospin. Under resonant conditions $\delta k_{2x}L = N\pi, N \in \mathbb{Z}$, the well also becomes totally transparent in K' valley. In the gap, T decreases exponentially. Deviations from theoretical predictions in Figs. 5.3 (b,d) with increasing frequency detuning are caused by non-linearality of the bands.

A series of COMSOL simulations were carried out for this system with different means of introduction of symmetry breaking into the structure. Panel (a) of Fig. 5.2 shows computed TM bands for the case when rods are identical and unmagnetized. The band diagram features band crossing near the edges of Bril-

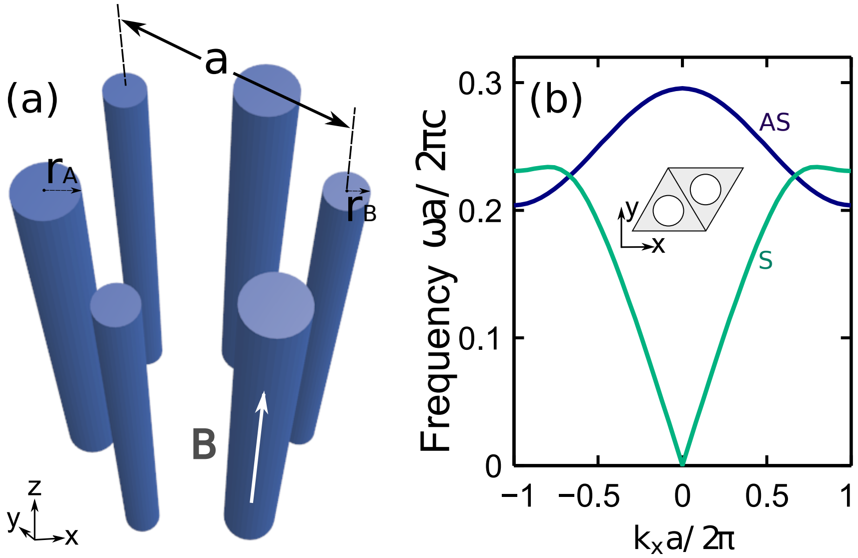

Figure 5.1: (a) Schematics of a honeycomb photonic crystal composed of ferromagnetic rods surrounded by air (b) Low-frequency photonic bands (TM) for a non-detuned crystal with no external magnetic field applied, $B = 0$. Inset in (b): a top view of a crystal unit cell comprising two identical cylinders. The dimensionless structure parameters are $r_A = r_B = 0.2$, $a = 1$, $\varepsilon_A = \varepsilon_B = 14$, $\mu = 2$. Dispersion curves of symmetric (S, green) and antisymmetric(AS, blue) modes.

louin zone with nearly linear dispersion that is reciprocal with respect to the direction (sign of vector k_x). This is to be expected because in this case there is no symmetry breaking. The Dirac-like dispersion emerges at $K = (4\pi/(3a))$ and $K' = (-4\pi/(3a))$

Panel (b) of Fig. 5.2 shows dispersion of the first nonreciprocal structure that exhibits two non-reciprocal Dirac cones that are slightly detuned in frequency. In this case, non-reciprocity is achieved by magnetizing the cylinders along z—axis in opposite directions thus breaking the TRS. Note, however, such magnetization preserves PT symmetry so that band crossings remain linear. Having the cylinders magnetized in opposite directions also ensures that the positions of Dirac cones are not shifted strongly. If the cylinders are magnetized in the same direction, same behaviour is observed, however the frequency of band crossing shifts dramatically. And finally panel (c) of Fig 5.2. shows one-way nonreciprocal response. In this case, symmetry breaking is achieved by introducing a small detuning in cylinder radii (SIS): $r_A = r + \delta/2$ and $r_B = r - \delta/2$. As was discussed earlier, it is possible to tune the parameter δ in such a way that the effects from magnetization and dimerization are canceled out for positive values of k_x near K point (forward propagation), thus, closing the gap, but amplified for negative values of k_x in the proximity of K' (backward propagation), opening the bandgap. The values used in the simulation are as follows: $\kappa = 0.54$ and $\delta = 0.009$.

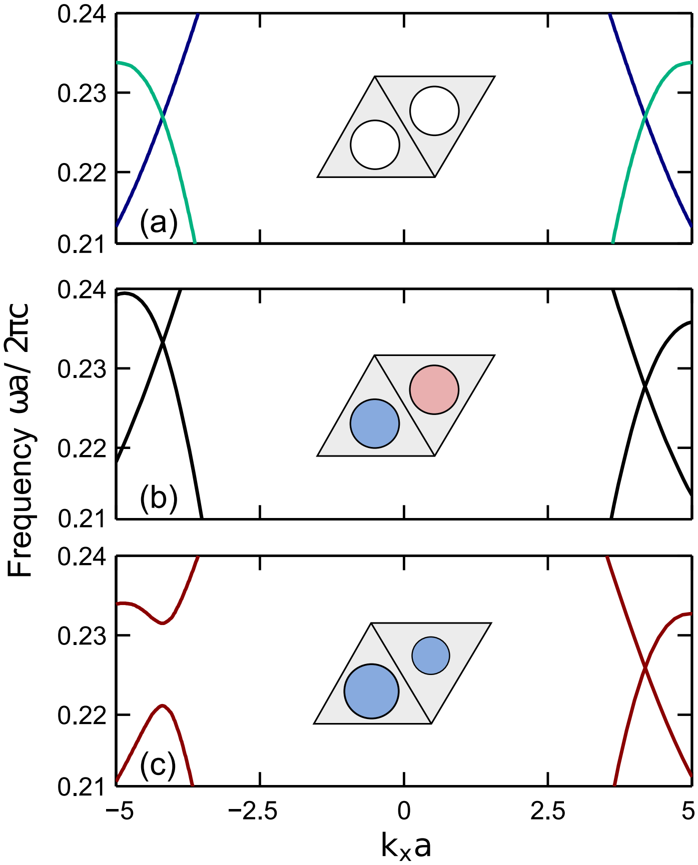

Figure 5.2: Dispersion near K and K' points for (a) a symmetric structure with non-magnetized rods, $\mu = 2$; (b) nonreciprocal PT-preserved crystal, cylinders of equal radii are magnetized in opposite directions, $mu = 2$, $\kappa = 0.6$; (c) nonreciprocal PT-violated crystal, cylinders of slightly detuned radii are magnetized in the same direction, $m = 1.8$, $\kappa = 0.54$, $\delta = r_A - r_B = 0.009$.

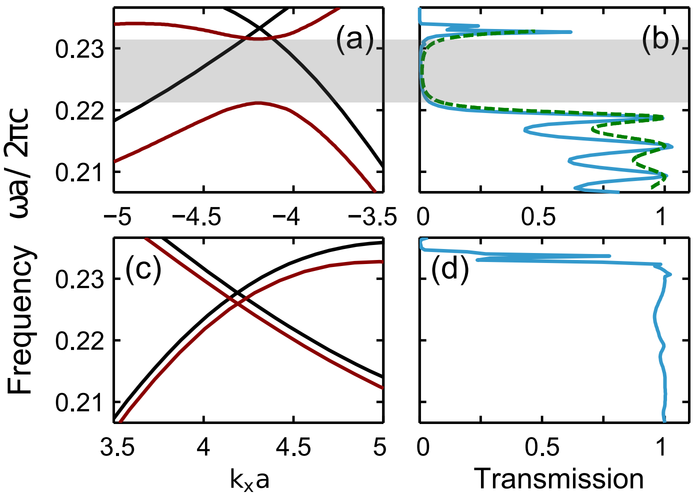

Figure 5.3: Photonic bands (a,c) and transmission coefficients (b,d). Panels (a,b) and (c,d) correspond to the backward and forward wave propagation, respectively. Red curves represent the structure shown in Fig 5.2 (c) while black curves represent the structure shown in Fig. 5.2. (b). Transmission calculated numerically is plotted with a blue line. The analytically retrieved transmission is depicted with green dashed line.

As can be seen from Fig. 5.3 (a,c) the two nonreciprocal structures in the spectral range of interest show crossed and gapped bands for negative values of k_x (Fig. 5.3(a)), and two overlapping Dirac cones for positive values of k_x (Fig. 5.3(c)). We used this non-reciprocal behavior of the photonic bandstructures to design a supercell that consists of three adjacent domains separated by zigzag cuts. The two side domains are constructed from the nonreciprocal PT-preserved crystal. The middle domain is made of nonreciprocal PT-violated crystal, and it effectively behaves as a potential well for propagating waves. To calculate the transmission through the potential well, we use a pair of current sheets located in the side regions that excite the eigen-modes of the structure.

As expected, the transmission is almost unity for the forward propagation, see Fig. 5.3(d). By contrast, for the backward propagation Fig. 5.3(b), the transmission rapidly declines to zero in the region of the gap which is consistent with the band structures shown in Fig. 3(a,c).

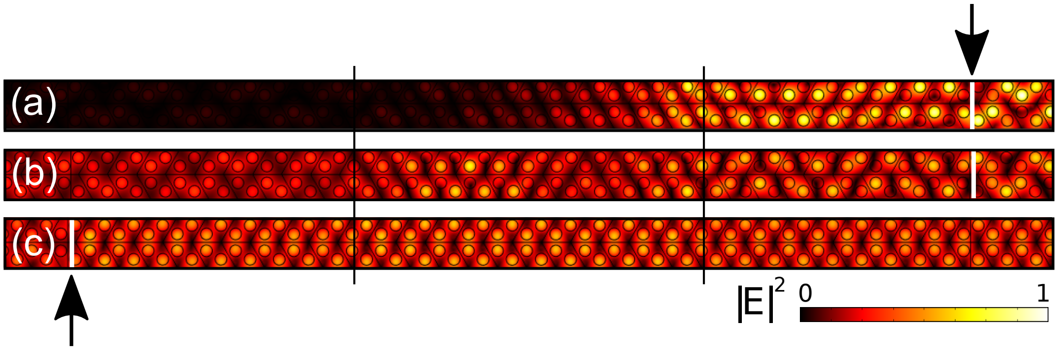

Figure 5.4: Simulated electric field intensity $| E |^2$ distributions in the strip for backward (top and middle panels) and forward (bottom panel) wave propagation. The strip consists of three domains, domain (1) is the nonreciprocal PT-preserving honeycomb lattices and separated by domain (2) composed of the inequivalent-sites lattice with magnetic field applied perpendicular to the lattice, and domains (1) and (2) contain 242 and 212 unit cells, respectively. The boundaries of three crystal regions are marked by black vertical lines. The modes are excited by current sheets at cuts indicated by the arrows and white lines.

Figure 5.4 demonstrates the field intensity $| E |^2$ profiles obtained from driven numerical simulations at different frequencies. In Figs. 5.4(a,b), the structure is excited by a sheet of electric current in the right domain as indicated by a black arrow. Hence, at the frequency falling in the gap, the excited wave experiences exponential decay in the gapped region and its tunneling to the left is suppressed.

At the lower frequency, a standing wave pattern tends to be formed in the middle region. Conversely, almost uniform field intensity distribution over the structure is seen in Fig. 5.4(c) for the case of forward propagation. The wave travels towards right without energy losses, featuring one-way Klein tunneling effect realized in this magneto-optical system.

5.3 Edge states in the continuum

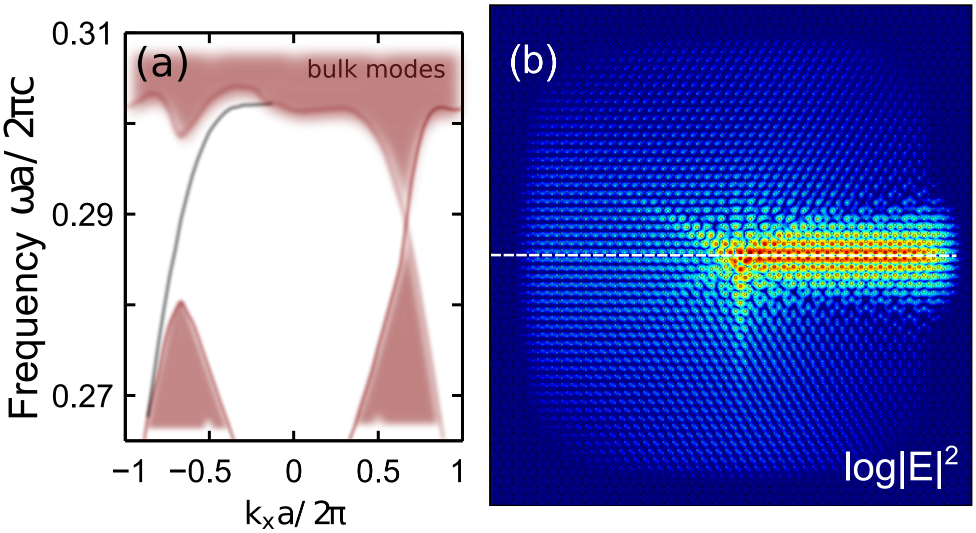

Figure 5.5: (a) Band diagram of 2D magnetic photonic crystal (shaded red) and a dispersion branch of the edge mode (grey curve) supported by the domain wall. (b) Numerically calculated field distribution in the crystal illustrating excitation of the one-way edge mode at the domain wall. The interface separating domains with masses of opposite signs is marked by a white line.

Finally, we perform first-principle numerical studies of the edge state residing in the bandgap of one of the valleys. This edge mode coexists spectrally with the gapless bulk continuum in K valley [see Fig. 5.5(a)]. The structure contains two domains (upper and lower) separated by a horizontal interface. The two domains are described by opposite mass terms: upper domain ($m_I = m_T = m$, lower domain ($m_I = m_T = -m$)). In Fig. 5.5(b) results of numerical modeling are demonstrated where the edge mode propagates one-way being excited by a point dipole source at the interface between two photonic crystals. To ensure reflectionless boundary conditions for propagating waves, materials losses are slowly added to the rods framing the simulation region.

6 Section E: Appendix

6.1 Notes to section C: Description of modes of conventional waveguide and their interaction with SSRs

In the absence of SSRs on top of the ferrite, the waveguide supports conventional modes that can be classified as TE and TM. When the ferrite is magnetized, oblique propagation (that is finite k_x) breaks the symmetry of the structure and causes splitting of TE and TM modes for positive and negative values of k_x.

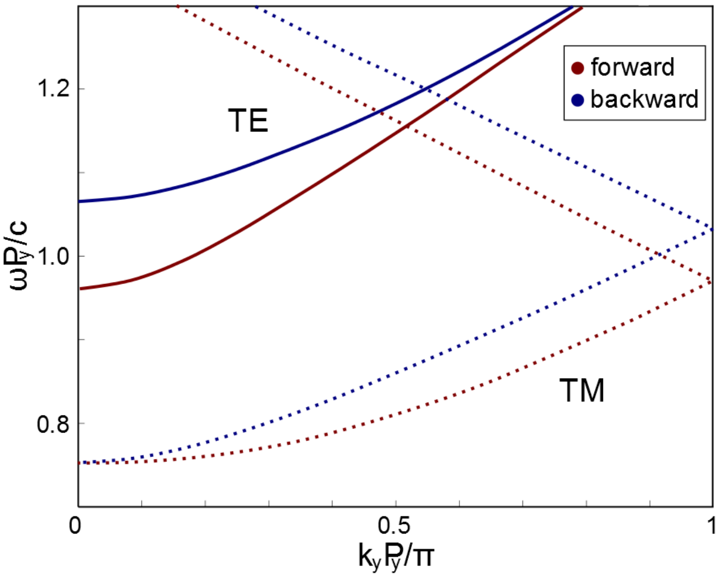

Figure 6.1: Band diagram for conventional waveguide shows TE(solid) and TM(dashed) modes.The modes split for forward(red,$k_x = 78.5m^{-1}$) and backward (blue,$k_x = -78.5m^{-1}$) propagation.

Field profile of each mode enables different interaction with SSRs once they are introduced on top of the ferrite. TE mode has magnetic field along z—

direction which excites the mangetic dipolar (dark) mode of the SSR. Conversely, TM mode has electric field along y— direction that interacts with the dipolar(bright) mode of the SSR. This effects can be seen in Fig.

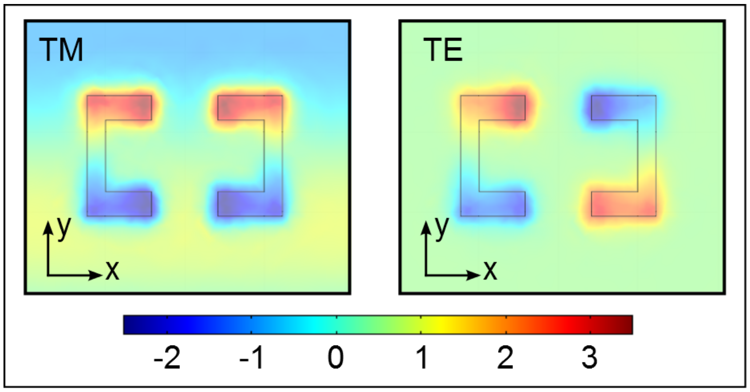

Figure 6.2: Out of plane electric field (E_z) distribution on top of the SSRs: for TM mode(left) and TE mode(right). TE mode excites the dark magnetic dipolar mode of the SSR, while TM mode excites the bright dipolar mode of the SSR.

6.2 Notes to section C: Comparison of SSR and square patch

The split ring resonator is needed to enhance interaction between TE and folded TM modes. For a fixed value of $k_x = 78.5m^{-1}$ two COMSOL simulations were carried out: (a) with SSR on top of the ferrite and (b) with a square element. In both cases, due to folding, a gap opens at the edge of the Brillouin zone. However, the gap emerging because of avoided crossing is almost 30 times wider for the SSR compared to the square element.

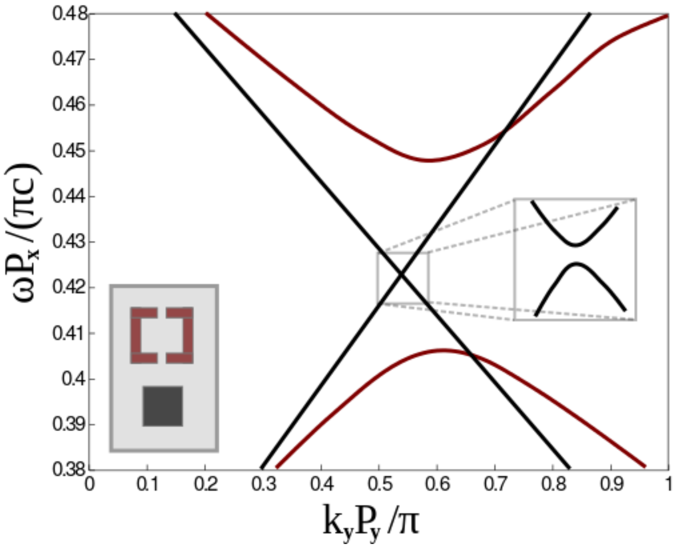

Figure 6.3: Comparison of bandgaps due to avoided crossing for: SSR (red) and square element (black)

6.3 Notes to section C:TCMT Analytical model describing non-reciprocal waveguide

The TCMT (temporal coupled mode theory) equations describing coupling between waveguide modes propagating inside the ferrite and metamolecule placed on top of it are given by the following expressions:

$$\dot{q} = i\omega_q q + \kappa_{qe} e + (\kappa_{qm}^{(1)}(\mu_{xz}) + \kappa_{qm}^{(2)}(k_x))m \tag{6.1}$$

$$\dot{e} = i\omega_e e + \kappa_{eq} q + \kappa_{em}^{(1)}(\mu_{xz})m \tag{6.2}$$

$$\dot{m} = i\omega_m m + (\kappa_{mq}^{(1)}(\mu_{xz}) + \kappa_{mq}^{(2)}(k_x))q + \kappa_{me}^{(1)}(\mu_{xz})e \tag{6.3}$$

Here the variables e and m characterize excitation strength of transverse electric(**TE**) and transverse magnetic (**TM**) waveguide modes respectively; q represents excitation of magnetic dipolar mode (**Q**) of the metamolecule. These variables are normalized in such a way that $|q|^2$,$|e|^2$ and $|m|^2$ represent energy stored in the respective mode. Parameters $\kappa_{mn} = -\kappa_{nm}^* = jK_{mn}$, define coupling strength between respective modes.

In the absence of magnetization the **TM** mode does not interact with either **TE** or **Q** modes; however the z-component of magnetic field of the **TE** mode enables its interaction with the metamolecule which results in hybridization of the two modes and gap opening; this interaction in described by the coupling parameter κ_{eq}.

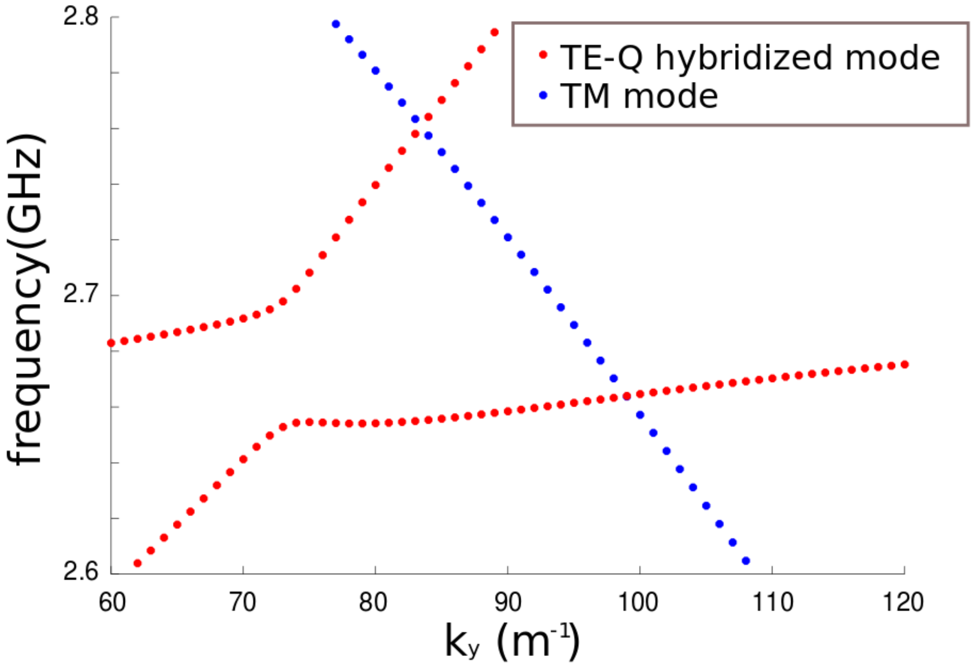

Figure 6.4: COMSOL numerical simulation. Band structure in the absence of magnetization shows the hybridized TE and Q modes (red) and folded TM mode (blue)

Coupling among other modes is achieved by means of symmetry breaking. Magnetizing the ferrite in y—direction causes the **TM** mode to gain a finite z-component of magnetic field and interact with the metamolecule effectively coupling **TM** and **Q** modes. When **TM** mode is not propagating strictly along y-axis, it possesses both x and y components of the electric field, which results into coupling between **TM** and **Q** modes. This interaction is described by set of parameters: $\kappa_{me}^{(1)}(\mu_{xz})$,$\kappa_{mq}^{(1)}(\mu_{xz})$ (magnetization) and $\kappa_{qm}^{(2)}(k_x)$(oblique propagation).

In order to quantitatively describe the spatial dispersion of this system in the vicinity of the region of interest ($k_y = [80, 120]m^{-1}$), we assume that the eigenfrequencies $\omega_e(k_y)$ and $\omega_m(k_y)$ are linear functions of k_y. On the other hand because the magnetic dipolar mode does not exhibit any spatial dispersion ω_q is assumed to be constant. As evidenced by small changes of the band structure with the introduction of magnetization, coupling coefficients are assumed to linearly depend on symmetry breaking parameters (μ_{xz} and k_x). The system can be solved for eigenfrequencies of hybrid modes as functions of k_y. To demonstrate that this model adequately describes the numerical simulation dispersion curves, the results of fitting are plotted in Fig. 5.2.

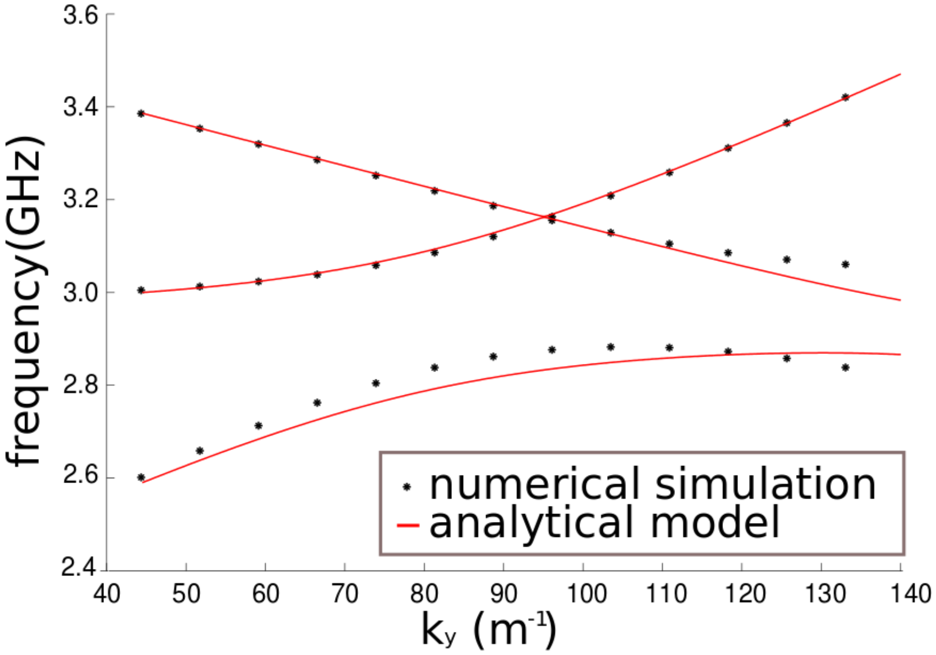

Figure 6.5: Results of numerical COMSOL simulation (dotted) fitted with analytical model(solid)

This model fully incorporates non-reciprocal behavior in our system for certain values of parameters which is in excellent agreement with simulation results.

This is illustrated in Fig. 5.3. As one can see the gap disappears as the sign of k_x is changed from positive to negative.

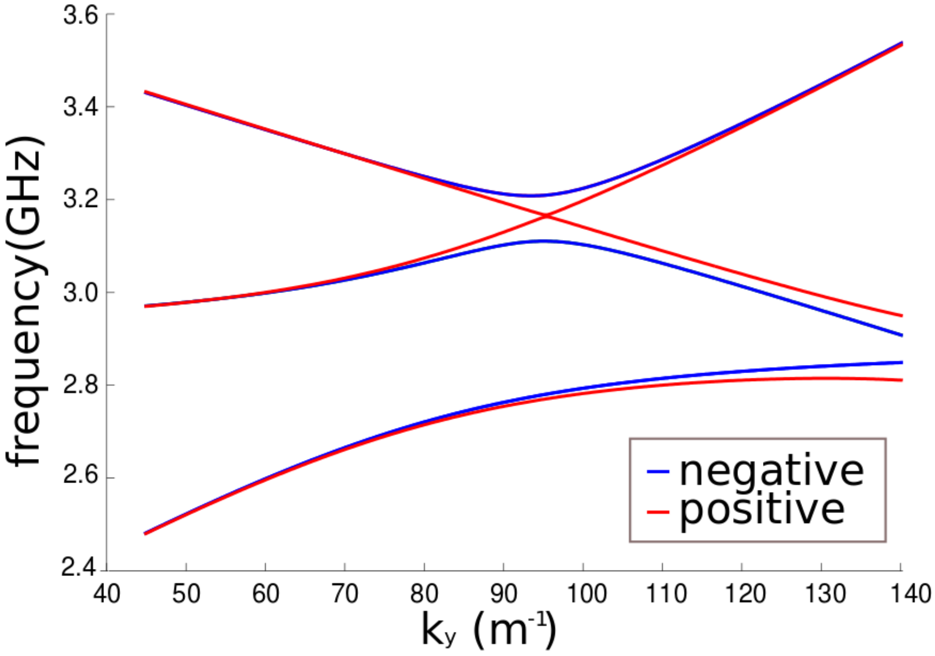

Figure 6.6: Analytical dispersion for $k_x = 78.5m^{-1}$ (red) and $k_x = -78.5^{-1}$ (blue) shows non-reciprocal behavior for opposite propagation directions

6.4 Notes to Section C: Structure parameters

Parameter	Value	Description
Px	0.02	Periodicity along x
Py	0.017	Periodicity along y
hFer	0.00917	Height of ferrite
aX	0.0011	Lenght of SSR
aY	0.0072	Width of SSR
aXp	0.02745	Width of clamps
aYp	0.001467	Height of clamps
dist	0.0088	Distance between left and right side of the SSR
muFer	2.25	Diagonal values of permeability tensor
k	1.45	Off diaognal values of permeability tensor
epsFer	12.9	Permittivity

6.5 Notes to Section D: Derivation of effective Hamiltonian

In this section, we derive the effective Hamiltonian in the vicinity of Dirac cones for a two dimensional honeycomb photonic crystal made of gyromagnetic cylinders using the plane wave expansion method. Assuming harmonic time dependency $\sim \exp(i\omega t)$, we start with Maxwell's equations,

$$\begin{aligned}\nabla \times \mathbf{E} &= -ik_0\hat{\mu}\mathbf{H}\,,\\ \nabla \times \mathbf{H} &= ik_0\varepsilon\mathbf{E}\,,\end{aligned} \tag{6.4}$$

where $k_0 = \omega/c$ is the wavevector in free space, ω is the angular frequency, and c is the speed of light. Material response is is described by effective parameters of a two-dimensional material:scalar permittivity ε and the permeability tensor containing off-diagonal conjugate imaginary components :

$$\hat{\mu} = \begin{pmatrix} \mu_\perp & i\varkappa & 0 \\ -i\varkappa & \mu_\perp & 0 \\ 0 & 0 & \mu_{zz} \end{pmatrix}. \tag{6.5}$$

Implying $\dfrac{\partial}{\partial z} = 0$, from Eq. (6.4) we obtain the governing equation for the $E_z(x,y)$ electric field component of TM polarization

$$\left(k_0^2\varepsilon + \frac{\partial}{\partial x}m\frac{\partial}{\partial x} + \frac{\partial}{\partial y}m\frac{\partial}{\partial y}\right)E_z = i\left(\frac{\partial}{\partial x}\Delta\frac{\partial}{\partial x} - \frac{\partial}{\partial y}\Delta\frac{\partial}{\partial y}\right)E_z\,, \tag{6.6}$$

where we have introduced compact notations $m = \dfrac{\mu_\perp}{\mu_\perp^2 - \varkappa^2}$ and $\Delta = \dfrac{\varkappa}{\mu_\perp^2 - \varkappa^2}$. Here, we assume in-plane propagation and the permittivity perturbed by a weak periodic modulation $\varepsilon = 1 + \tilde{\varepsilon}$. Given the crystal periodicity, we apply Bloch theorem and expand the electric field E_z and the constitutive parameters in Fourier series as follows,

$$E_z = \sum_G E_{\mathbf{G}} \, e^{i(\mathbf{G}+\mathbf{q})\cdot\mathbf{r}}\,, \tag{6.7}$$

$$\{\tilde{\varepsilon}, m, \Delta\} = \sum_G \{\tilde{\varepsilon}_{\mathbf{G}}, m_{\mathbf{G}}, \Delta_{\mathbf{G}}\} \, e^{i\mathbf{G}\cdot\mathbf{r}}\,, \tag{6.8}$$

where $\mathbf{G}$ and $\mathbf{G}'$ are the reciprocal lattice vectors. The length of all reciprocal lattice vectors $\mathbf{G}_i$ is equal to $G = 4\pi/(\sqrt{3}a)$, where a is a lattice constant of the crystal. Substituting Eqs. (6.7), (6.8) into Eq. (6.6), a set of linear equations for the Fourier components of the field is obtained:

$$\begin{aligned} &k_0^2 E_{\mathbf{G}} + k_0^2 \sum_{G'} \tilde{\varepsilon}_{\mathbf{G}-\mathbf{G}'} E_{\mathbf{G}'} - \sum_{G'} m_{\mathbf{G}-\mathbf{G}'} (\mathbf{q}+\mathbf{G})\cdot(\mathbf{q}+\mathbf{G}') E_{\mathbf{G}'} = \\ &-i \sum_{G'} \Delta_{\mathbf{G}-\mathbf{G}'} \left[(q_x + G_x)(q_y + G'_y) - (q_x + G'_x)(q_y + G_y) \right] E_{\mathbf{G}'} \end{aligned} \tag{6.9}$$

We are now interested in dispersion of the modes near the K (K') points at the edge of the Brillouin zone, which correspond to the Bloch wavevectors $\mathbf{K}_\pm = K(\pm 1, 0, 0)$, where $K = \dfrac{4\pi}{3a}$, so that for the K (K') valleys $\mathbf{q} + \mathbf{G} = \mathbf{K}_\pm + \delta\mathbf{k} + \mathbf{G} \equiv \mathbf{k} + \delta\mathbf{k}$, where $\delta\mathbf{k}$ is a small detuning. We truncate the basis to the first three plane waves with the wavevectors $\mathbf{k}_{1,2,3} = \mathbf{K}_\pm + \mathbf{G}_{0,1,2}$ each rotated by $2\pi/3$ with respect to one another and corresponding to the reciprocal lattice vectors

$\mathbf{G}_0 = (0,0)$, $\mathbf{G}_1 = K\left(\mp\frac{3}{2}, -\frac{\sqrt{3}}{2}\right)$, $\mathbf{G}_2 = K\left(\mp\frac{3}{2}, \frac{\sqrt{3}}{2}\right)$. Thus, to describe the formation of the bands, we leave only the leading contributions from three Γ points nearest to K (K') with $\mathbf{k}_1 = (\pm K, 0)$, $\mathbf{k}_2 = K\left(\mp\frac{1}{2}, -\frac{\sqrt{3}}{2}\right)$, $\mathbf{k}_3 = K\left(\mp\frac{1}{2}, \frac{\sqrt{3}}{2}\right)$. Next, we apply $k \cdot p$ approximation, keeping only the first order terms in $\delta\mathbf{k}$, $(\mathbf{k}_i + \delta\mathbf{k}) \cdot (\mathbf{k}_j + \delta\mathbf{k}) \approx \mathbf{k}_i \cdot \mathbf{k}_j + \delta\mathbf{k} \cdot (\mathbf{k}_i + \mathbf{k}_j)$. Neglecting the terms of higher orders, we obtain a 3×3 set of equations

$$\Bigg[k_0^2 \begin{pmatrix} 1+\tilde{\varepsilon}_0 & \tilde{\varepsilon}_{01} & \tilde{\varepsilon}_{02} \\ \tilde{\varepsilon}_{01}^* & 1+\tilde{\varepsilon}_0 & \tilde{\varepsilon}_{12} \\ \tilde{\varepsilon}_{02}^* & \tilde{\varepsilon}_{12}^* & 1+\tilde{\varepsilon}_0 \end{pmatrix} - \begin{pmatrix} m_0\mathbf{k}_1^2 & m_{01}(\mathbf{k}_1\cdot\mathbf{k}_2) & m_{02}(\mathbf{k}_1\cdot\mathbf{k}_3) \\ m_{01}^*(\mathbf{k}_1\cdot\mathbf{k}_2) & m_0\mathbf{k}_2^2 & m_{12}(\mathbf{k}_2\cdot\mathbf{k}_3) \\ m*_{02}(\mathbf{k}_1\cdot\mathbf{k}_3) & m_{12}^*(\mathbf{k}_2\cdot\mathbf{k}_3) & m_0\mathbf{k}_3^2 \end{pmatrix}$$

$$-\delta\mathbf{k}\cdot \begin{pmatrix} 2\mathbf{k}_1 m_0 & (\mathbf{k}_1+\mathbf{k}_2)m_{01} & (\mathbf{k}_1+\mathbf{k}_3)m_{02} \\ (\mathbf{k}_1+\mathbf{k}_2)m_{01}^* & 2\mathbf{k}_2 m_0 & (\mathbf{k}_2+\mathbf{k}_3)m_{12} \\ (\mathbf{k}_1+\mathbf{k}_3)m_{02}^* & (\mathbf{k}_2+\mathbf{k}_3)m_{12}^* & 2\mathbf{k}_3 m_0 \end{pmatrix}$$

$$+i \begin{pmatrix} 0 & [\mathbf{k}_1\times\mathbf{k}_2]_z\Delta_{01} & [\mathbf{k}_1\times\mathbf{k}_3]_z\Delta_{02} \\ [\mathbf{k}_1\times\mathbf{k}_2]_z\Delta_{01}^* & 0 & [\mathbf{k}_2\times\mathbf{k}_3]_z\Delta_{12} \\ [\mathbf{k}_1\times\mathbf{k}_3]_z\Delta_{02}^* & [\mathbf{k}_2\times\mathbf{k}_3]_z\Delta_{12}^* & 0 \end{pmatrix}\Bigg] \begin{pmatrix} E_{\mathbf{G}_0} \\ E_{\mathbf{G}_1} \\ E_{\mathbf{G}_2} \end{pmatrix} = 0.$$

The Fourier coefficients are defined as

$$\{\tilde{\varepsilon},m,\Delta\}_{ij}=\frac{1}{S_0}\int\limits_{\text{u.c.}}\{\tilde{\varepsilon},m,\Delta\}(x,y)\,e^{-i\left(\mathbf{G}_i-\mathbf{G}_j\right)\cdot\mathbf{r}}\,d^2\mathbf{r}_\perp\,, \tag{6.10}$$

where $S_0=a^2\sqrt{3}/2$ is the area of the structure unit cell, and the index $\left(\mathbf{G}_i-\mathbf{G}_j\right)\equiv\mathbf{G}_{ij}$ is abbreviated as ij. In particular, coefficients $\{\tilde{\varepsilon},m,\Delta\}_{00,11,22}\equiv\{\tilde{\varepsilon},m,\Delta\}_0$ imply averaged over the unit cell spatial distributions. Additionally, we make use of a honeycomb symmetry of the lattice. To take into account a slight difference of two rods A and B in the unit cell, we write

$$\{\tilde{\varepsilon},m,\Delta\}(\mathbf{r}_\perp)=\left(\left\{\bar{\tilde{\varepsilon}},\bar{m},\bar{\Delta}\right\}-\frac{1}{2}\delta\{\tilde{\varepsilon},m,\Delta\}\right)\sqcap(\mathbf{r}_\perp-\mathbf{v}_1)+\left(\left\{\bar{\tilde{\varepsilon}},\bar{m},\bar{\Delta}\right\}+\frac{1}{2}\delta\{\tilde{\varepsilon},m,\Delta\}\right)\sqcap(\mathbf{r}_\perp+\mathbf{v}_1), \tag{6.11}$$

where $\mathbf{v}_1=\mathbf{r}_{\text{AB}}/2$, and functions $\sqcap(\mathbf{r}_\perp\pm\mathbf{v}_1)$ are localized on the lattice sites. Thereby, expression (6.12) takes the form

$$\{\tilde{\varepsilon},m,\Delta\}_{ij}=\frac{I_1}{S_0}\left(\left\{\bar{\tilde{\varepsilon}},\bar{m},\bar{\Delta}\right\}2\cos\varphi_{ij}+i\delta\{\tilde{\varepsilon},m,\Delta\}\sin\varphi_{ij}\right)\equiv\{\tilde{\varepsilon},m,\Delta\}_1\cos\varphi_{ij}+i\delta\{\tilde{\varepsilon},m,\Delta\}_{\text{AB}}\sin\varphi_{ij}\,, \tag{6.12}$$

where $\varphi_{ij}=(\mathbf{G}_{ij}\cdot\mathbf{v}_1)$. Choosing $\mathbf{v}_1=\left(-\dfrac{\sqrt{3}}{2},\dfrac{1}{2}\right)d$, where $d=\dfrac{a}{\sqrt{3}}$ is a distance between cylinders A and B , we calculate the angles $\varphi_{01}=\varphi_{12}=-\varphi_{21}=-\varphi_{10}=-\pi/3$, $\varphi_{02}=-2\pi/3=-\varphi_{20}$. Finally, in the case of codirectional magnetization, we reach a set of equations

$$k_0^2(1+\hat{\varepsilon})\mathscr{E}=\left(\hat{m}+\hat{m}_{AB}+\hat{\theta}\right)\mathscr{E}, \tag{6.13}$$

where the column-vector $\mathscr{E} = (E_{\mathbf{G}_0}, E_{\mathbf{G}_1}, E_{\mathbf{G}_2})^{\mathrm{T}}$, and 3×3 matrices are given by

$$\begin{aligned}\hat{m} = K^2 \begin{pmatrix} m_0 & -\frac{1}{2}m_1 & \frac{1}{2}m_1 \\ -\frac{1}{2}m_1 & m_0 & -\frac{1}{2}m_1 \\ \frac{1}{2}m_1 & -\frac{1}{2}m_1 & m_0 \end{pmatrix} \pm K\delta k_x \begin{pmatrix} 2m_0 & \frac{1}{2}m_1 & -\frac{1}{2}m_1 \\ \frac{1}{2}m_1 & -m_0 & -m_1 \\ -\frac{1}{2}m_1 & -m_1 & -m_0 \end{pmatrix} \\ + K\delta k_y \begin{pmatrix} 0 & -\frac{\sqrt{3}}{2}m_1 & -\frac{\sqrt{3}}{2}m_1 \\ -\frac{\sqrt{3}}{2}m_1 & -\sqrt{3}m_0 & 0 \\ -\frac{\sqrt{3}}{2}m_1 & 0 & \sqrt{3}m_0 \end{pmatrix},\end{aligned}$$

$$\hat{m}_{AB} = i\delta m_{\mathrm{AB}} K^2 \begin{pmatrix} 0 & -\frac{\sqrt{3}}{2} & -\frac{\sqrt{3}}{2} \\ \frac{\sqrt{3}}{2} & 0 & -\frac{\sqrt{3}}{2} \\ \frac{\sqrt{3}}{2} & \frac{\sqrt{3}}{2} & 0 \end{pmatrix}$$

$$\hat{\theta} = \mp i\Delta_1 K^2 \begin{pmatrix} 0 & -\frac{\sqrt{3}}{2} & -\frac{\sqrt{3}}{2} \\ \frac{\sqrt{3}}{2} & 0 & -\frac{\sqrt{3}}{2} \\ \frac{\sqrt{3}}{2} & \frac{\sqrt{3}}{2} & 0 \end{pmatrix} \tag{6.14}$$

$$\hat{\varepsilon} = \begin{pmatrix} \tilde{\varepsilon}_0 & \tilde{\varepsilon}_1 & -\tilde{\varepsilon}_1 \\ \tilde{\varepsilon}_1 & \tilde{\varepsilon}_0 & \tilde{\varepsilon}_{12} \\ -\tilde{\varepsilon}_1 & \tilde{\varepsilon}_1 & \tilde{\varepsilon}_0 \end{pmatrix}.$$

Thus, we obtain 3×3 eigenvalue problem, $k_0^2 \mathscr{E} = (1+\hat{\varepsilon})^{-1} \left(\hat{m} + \hat{m}_{AB} + \hat{\theta}\right) \mathscr{E} = \hat{H}_1 \mathscr{E}$.

After performing a unitary transformation $\hat{H} = U \hat{H}_1 U^{-1}$ with the matrix

$$U = \frac{1}{\sqrt{3}} \begin{pmatrix} 1 & e^{i\pi/3} & e^{2i\pi/3} \\ 1 & e^{-i\pi/3} & e^{-2i\pi/3} \\ e^{i\pi/3} & e^{-2i\pi/3} & e^{i\pi/3} \end{pmatrix}, \tag{6.15}$$

we note that the third row of the transformed matrix describes a nondegenerate singlet TM state, and therefore it can be eliminated. Thus, we recover the following effective massive Dirac Hamiltonian in the subspace of the doublet states

$$\hat{H}_{K(K')} = \Omega_0 \pm V\delta k_x \hat{\sigma}_x + V\delta k_y \hat{\sigma}_y + (\pm m_{\mathrm{T}} - m_{\mathrm{I}})\hat{\sigma}_z \,, \tag{6.16}$$

where the unperturbed frequency $\Omega_0 = \dfrac{K^2\left(m_0 - \dfrac{1}{2}m_1\right)}{1+\tilde{\varepsilon}_0+\tilde{\varepsilon}_1}$, velocities $V = \dfrac{K(m_0+m_1)}{1+\tilde{\varepsilon}_0+\tilde{\varepsilon}_1}$, and mass terms due to parity breaking $m_{\mathrm{I}} = \dfrac{3K^2\delta m_{\mathrm{AB}}}{2(1+\tilde{\varepsilon}_0+\tilde{\varepsilon}_1)}$, and time-reversal symmetry breaking $m_{\mathrm{T}} = \dfrac{3K^2\Delta_1}{2(1+\tilde{\varepsilon}_0+\tilde{\varepsilon}_1)}$.

For the case of oppositely magnetized cylinders, in place of imaginary matrices $\hat{m}_{AB}$ and $\hat{\theta}$, we have a real matrix

$$U = \frac{3}{4}K^2\delta\Delta_{\mathrm{AB}}\begin{pmatrix} 0 & \pm 1 & \mp 1 \\ \pm 1 & 0 & \pm 1 \\ \mp 1 & \pm 1 & 0 \end{pmatrix} , \tag{6.17}$$

leading to the Dirac Hamiltonians

$$\hat{H}_{K(K')} = \Omega_0 \pm \delta\Omega_0 \pm V\delta k_x \hat{\sigma}_x + V\delta k_y \hat{\sigma}_y \,, \tag{6.18}$$

with opposite frequency detunings $\delta\Omega_0 = \dfrac{3}{4}K^2\delta\Delta_{\mathrm{AB}}$ in different valleys.

6.6 Notes to section D: Nonreciprocal tunneling in photonic graphene with a single potential barrier

Depending on relative values of Ω, u_2 and m_2, formula (5.4) of the main text can be split into two cases that we write out now explicitly:

$$T(\Omega) = \frac{1}{\left(1+\frac{1}{4}\sinh^2(\kappa_{2x}L)\left[\frac{s_1}{c_2}+\frac{c_2}{s_1}\right]^2\right)}\,, \quad \text{if} \quad m_2^2 > (\Omega-u_2)^2\,, \tag{6.19a}$$

$$T(\Omega) = \frac{1}{\left(1+\frac{1}{4}\sin^2(k_{2x}L)\left[\frac{s_1}{s_2}-\frac{s_2}{s_1}\right]^2\right)}\,, \quad \text{if} \quad m_2^2 < (\Omega-u_2)^2\,, \quad , \tag{6.19b}$$

where $s_1 = \sqrt{\Omega^2-m_1^2}/(\Omega-m_1)$, $c_2 = \sqrt{m_2^2-(\Omega-u_2)^2}/(\Omega-u_2-m_2)$, $s_2 = \sqrt{(\Omega-u_2)^2-m_2^2}/(\Omega-u_2-m_2)$, $\kappa_{2x} = \sqrt{m_2^2-(\Omega-u_2)^2}/V$, $k_{2x} = \sqrt{(\Omega-u_2)^2-m_2^2}/V$. Here, we set $u_1 = 0$ and assume $\Omega^2 > m_1^2$. In particular, (i) the trivial case $u_2 = 0$ (no barrier), and (ii) setting $m_2 = m_1 = 0$ (Klein paradox) return unity transmission.

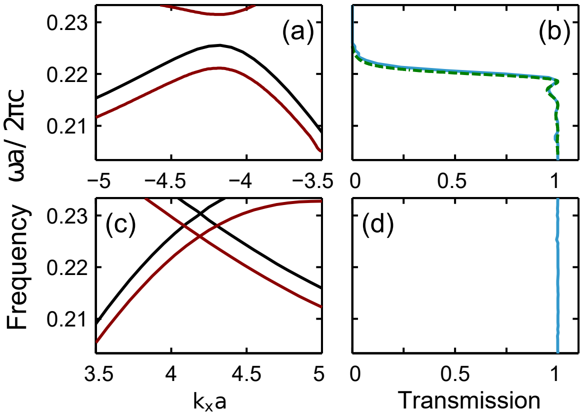

Figure 6.7: (Color online) Photonic bands (a,c) and transmission coefficients (b,d) for $1/2/1$ supercell made of the gapped nonreciprocal crystals with $m_1 = m_2 = m$. Panels (a,b) and (c,d) correspond to the backward and forward wave propagation, respectively. Transmission calculated numerically is plotted with a blue line. Green dashed curve is the analytically retrieved dependence.

Figure 6.7 presents additional calculated results for nonreciprocal tunneling in the case where the side domains 1 and the middle domain 2 are all made of PT-violated gapped crystals.

List of Publications

1. N. Arju, T. Ma, A. B. Khanikaev, D. Purtseladze, G. Shvets, Optical Realization of Double-Continuum Fano Interference and Coherent Control in Plasmonic Metasurfaces, Phys. Rev. Lett. 114 (23), 237403, (2015)

2. S. H. Mousavi, I. Kholmanov, K. Alici, D. Purtseladze, David Y. Fozdar, Y. Hao, A. B. Khanikaev, R. S. Ruoff, and G. Shvets, Inductive Tuning of Fano-Resonant Meta-Surfaces Using Plasmonic Response of Graphene in Mid-Infrared, Nano Letters 13 (3), 11111117 (2013)

3. A. B. Khanikaev, N. Arju, Z. Fan, D. Purtseladze, F. Lu, J. Le , P. Sarriugarte, M. Schnell, R. Hillenbrand, M. Belkin, Experimental demonstration of the microscopic origin of circular dichroism in two-dimensional metamaterials, Nature Communications 7, 12045 (2016)

4. Spin and valley polarized one-way Klein tunneling in photonic topological insulators

Bibliography

[1] J.B. Pendry. “Negative refraction”. In: *Contemporary Physics* 45.3 (2004), pp. 191–202. DOI: `10.1080/00107510410001667434`.

[2] Veselago V.G. In: *Soviet Physics USPEKHI* 10.509 (1968).

[3] Potton R. J. “Reciprocity in optics”. In: *Rep. Prog. Phys.* 67 (2004), p. 717.

[4] Pozar D. “Microwave Engineering”. In: *4 edition Wiley, Hoboken, New Jersey* 67 (2011).

[5] Mousavi S.H., Khanikaev A.B., Allen J. and Allen M., Shvets G. “Gyromagnetically induced transparency of Metasurfaces”. In: *Phys. Rev. Lett.* 112 (2014), p. 117402.

[6] Chihhui Wu, Alexander B. Khanikaev and Gennady Shvets. “Broadband Slow Light Metamaterial Based on a Double-Continuum Fano Resonance”. In: *Phys. Rev. Lett.* 106.107403 (2011).

[7] Shuang Zhang et. al. “Plasmon-Induced Transparency in Metamaterials”. In: *Phys. Rev. Lett.* 101.047401 (2008).

[8] Zhao Y. and A. Alu. “Manipulating light polarization with ultrathin plasmonic metasurfaces”. In: *Phys. Rev. B* 84.205428 (2011).

[9] Khanikaev A. B. et al. “Electromagnetically induced polarization conversion.” In: *Opt. Commun.* 285 (2012), pp. 3423–3427.

[10] Wang D., et al. “An ultrathin terahertz quarter-wave plate using planar babinet-inverted metasurface”. In: *Opt. Express* 23 (2015), pp. 11114–11122.

[11] Khoo E. H., Li E. P. and Crozier K. B. “Plasmonic wave plate based on subwavelength nanoslits”. In: *Opt. Lett.* 36 (2011), pp. 2498–2500.

[12] Zhao Y., Belkin M. A., Alu A. “Twisted optical metamaterials for planarized ultrathin broadband circular polarizers”. In: *Nat. Commun.* 3.870 (2012).

[13] Gansel J. K. et al. “Gold helix photonic metamaterial as broadband circular polarizer”. In: *Science* 325 (2009), pp. 1513–1515.

[14] Rakic A. D., Djurisic A. B., Elazar J. M. and Majewski M. L. “Optical properties of metallic films for vertical-cavity optoelectronic devices”. In: *Appl. Opt.* 37 (1998), pp. 5271–5283.

[15] Fedotov V.A. et al. “Asymmetric propagation of electromagnetic waves through a planar chiral structure.” In: *Phys. Rev. Lett.* 97.167401 (2006).

[16] Arju N., Ma T., Khanikaev A. and Purtseladze D., Shvets G. “Optical realization of double-continuum fano interference and coherent control in plasmonic metasurfaces.” In: *Phys. Rev. Lett.* 114.237403 (2015).

[17] Dazzi A., Prazeres R., Glotin F. and Ortega J. M. “Local infrared microspectroscopy with subwavelength spatial resolution with an atomic force microscope tip used as a photothermal sensor.” In: *Opt. Lett.* 30 (2005), pp. 2388–2390.

[18] Lu F. and Belkin M. A. “Infrared absorption nano-spectroscopy using sample photoexpansion induced by tunable quantum cascade lasers.” In: *Opt. Express* 19 (2011), pp. 19942–19947.

[19] Lu F., Jin M and Belkin M. A. “Tip-enhanced infrared nanospectroscopy via molecular expansion force detection”. In: *Nat. Photon.* 8 (2014), pp. 307–312.

[20] Fano U. “Effects of configuration interaction on intensities and phase shifts.” In: *Phys. Rev.* 124 (1961), pp. 1866–1878.

[21] Fan S., Suh W. and Joannopoulos J. D. “Temporal coupled-mode theory for the Fano resonance in optical resonators”. In: *JOSA A* 20 (2003), p. 569.

[22] Fedotov V., et al. “Sharp Trapped-Mode Resonances in Planar Metamaterials with a Broken Structural Symmetry”. In: *Phys. Rev. Lett.* 99 (2007), p. 147401.

[23] Lukyanchuk B. et al. “The Fano resonance in plasmonic nanostructures and metamaterials”. In: *Nat. Mater.* 9 (2010), pp. 707–715.

[24] Liu N. et al. “Plasmonic analogue of electromagnetically induced transparency at the Drude damping limit.” In: *Nat. Mater.* 8 (2009), pp. 758–762.

[25] Miroshnichenko A., Flach S. and Kivshar Y. “Fano resonances in nanoscale structures.” In: *Rev. Mod. Phys.* (2010), pp. 1–42.

[26] Chung-Yen Chao and L. Jay Guo. “Biochemical sensors based on polymer microrings with sharp asymmetrical resonance”. In: *Appl. Phys. Lett.* 83 (2003), pp. 1527–1529.

[27] Hao F. et al. “Symmetry Breaking in Plasmonic Nanocavities: Subradiant LSPR Sensing and a Tunable Fano Resonance.” In: *Nano Lett.* 8 (2008), pp. 3983–3988.

[28] Bennink R. S. et al. “Accessing the optical nonlinearity of metals with metal-dielectric photonic bandgap structures.” In: *Opt. Lett.* 24 (1999), p. 1416.

[29] Pendry J.B., Holden A.J.,Robbins D.J. and Stewart W.J. “Magnetism from conductors and enhanced nonlinear phenomena”. In: *IEEE Trans. Microw. Theory Tech.* 47 (1999), pp. 2075–2084.

[30] Khanikaev A. B., Wu C. and Shvets G. “Fano-resonant metamaterials and their applications”. In: *Nanophotonics 2* 247 (2013).

[31] Gallinet B. and Martin O. J. F. “Ab initio theory of Fano resonances in plasmonic nanostructures and metamaterials”. In: *Phys. Rev. B* 83 (2011), p. 235427.

[32] Haus H. “Waves and Fields in Optoelectronics”. In: *Prentice-Hall:Englewood Cliffs, NJ,* (1984).

[33] Zvezdin A.K., Kotov V.A. “Modern Magnetooptics and Magnetooptical Materials”. In: *CNRS Press, Paris* (1997).

[34] Harris V.G. “Modern Microwave Ferrites”. In: *IEEE Transactions on Magnetics* 48 (2012), pp. 1075–1104.

[35] Khanikaev A.B., Mousavi S.H., Shvets G. and Kivshar Yu. S. “One-way extraordinary optical transmission and nonreciprocal spoof plasmons”. In: *Phys. Rev. Lett.* 105 (2010), p. 126804.

[36] Khanikaev A.B., Baryshev M., Inoue M. and Kivshar Yu.S. “One-way electromagnetic Tamm states in magnetophotonic structures”. In: *Appl. Phys. Lett.* 95 (2009), p. 011101.

[37] Khanikaev A.B. and Steel M.J. “Low-symmetry magnetic photonic crystals for nonreciprocal and unidirectional devices”. In: *Optc. Express* 17 (2009), p. 5265.

[38] Klein O. “Die Reflexion von Elektronen an einem Potentialsprung nach der relativistischen Dynamik von Dirac”. In: *Zeitschrift fur Physik* 53.3-4 (1929), p. 157.

[39] Andrea F. Young and Philip Kim. “Quantum interference and Klein tunnelling in graphene heterojunctions”. In: *Nature Phys* (2009), pp. 222–226.

[40] Novoselov K.S. “Electric field effect in atomically thin carbon films”. In: *Science* 306 (2004), pp. 666–669.

[41] Novoselov K.S. “Katsnelson M.I, Novoselov K.S. and Geim A.K.” In: *Nature Phys. 2* (2006), pp. 620–625.

[42] C. W. J. Beenakker. “Colloquium: Andreev reflection and klein tunneling in graphene”. In: *Rev. Mod. Phys.* 80 (2008), pp. 1337–1354.

[43] Robinson T.R. “On Klein tunneling in graphene”. In: *Am. J. Phys.* 80 (2012), pp. 141–147.

[44] Alexander Szameit, Mikael C. Rechtsman, Omri Bahat-Treidel and Mordechai Segev. “PT-symmetry in honeycomb photonic lattices”. In: *Phys. Rev. A* 84 (2011), p. 021806.

[45] Mikael C. Rechtsman et. al. “Photonic Floquet topological insulators”. In: *Nature 496* (2013), pp. 196–200.

[46] Lu L., Joannopoulos J.D. and Soljacic M. “Topological photonics”. In: *Nature Photon.* 8 (2014), pp. 821–829.

[47] Lu L., Joannopoulos J.D. and Soljacic M. “Topological states in photonic systems”. In: *Nature Phys.* 12 (2016), p. 626.

[48] S. Raghu and Haldane F. D. M. “Analogs of quantum-Hall-effect edge states in photonic crystals”. In: *Phys. Rev. A* 78 (2008), p. 033834.

[49] Ma T., Shvets G. “All-Si valley-hall photonic topological insulator”. In: *New J. Phys* 18 (2016), p. 025012.

Vita

David Purtseladze attended Illia Vekua School of Physics and Mathematics and Georgian Lyceum of Science and Technology in Tbilisi, Georgia. Then he began his undergraduate studies at the Moscow Instutute of Physics and Technology in Moscow, Russia. He was performing research at Lebedev Physical Institute under the supervision of professor Alexander Urnov and earned his Bachelor of Science and Master of Science degrees. He then moved to Austin to pursue his doctoral degree in Physics. From 2011-2015 he worked for Gennady Shvets as a graduate research assistant and taught multiple undergraduate laboratory and discussion classes. From 2015-2017 he worked under the supervision of Alexander Khanikaev and Richard Fitzpatrick.

Permanent address: 1020 E 45th street, APT 243, Austin, TX, 78751

This dissertation was typeset by the author.